American Mineralogist, Volume 107, pages 1116–1132, 2022

Timescales and rates of intrusive and metamorphic processes determined from zircon and garnet in migmatitic granulite, Fiordland, New Zealand

HAROLD STOWELL[1,*], JOSHUA SCHWARTZ[2,†], ELIZABETH BOLLEN[1], ANDY TULLOCH[3],
JAHANDAR RAMEZANI[4], AND KEITH KLEPEIS[5]

[1]Geological Sciences, University of Alabama, Tuscaloosa, Alabama 35487-0338, U.S.A.
[2]Geological Sciences, California State University Northridge, Northridge, California 91330, U.S.A.
[3]GNS Science 764 Cumberland Street, Dunedin 9016, Private Bag 1930, Dunedin 9054, New Zealand
[4]Earth, Atmospheric and Planetary Science, Massachusetts Institute of Technology, Cambridge, Massachusetts 02139, U.S.A.
[5]Department of Geology, University of Vermont, 180 Colchester Avenue, Burlington, Vermont 05405, U.S.A.

ABSTRACT

Zircon U-Pb, and garnet Sm-Nd and Lu-Hf dates provide important constraints on local and orogenic scale processes in lower-crustal rocks. However, in high-temperature metamorphic rocks these isotopic systems typically yield significant ranges reflecting both igneous and metamorphic processes. Therefore, linking dates to specific aspects of rock history can be problematic. In Fiordland, New Zealand, granulite-facies orthogneiss is cut by leucosomes that are bordered by garnet clinopyroxene reaction zones (garnet reaction zones). In both host orthogneiss and garnet reaction zones, zircon are typically anhedral with U-Pb dates ranging from 118.30 ± 0.13 to 115.70 ± 0.18 Ma (CA-ID-TIMS) and 121.4 ± 2.0 to 109.8 ± 1.8 Ma (SHRIMP-RG). Zircon dates in host and garnet reaction zone do not define distinct populations. In addition, the dates cannot be readily grouped based on external morphology or internal CL zoning. Zircon trace-element concentrations indicate two distinct crystallization trends, clearly seen in Th and U. Garnet occurs in selvages to the leucosome veins and in the adjacent garnet reaction zones. In selvages and host orthogneiss, garnet is generally 0.5 to 1 cm diameter and euhedral and is 0.1 to 0.5 cm diameter and subhedral in garnet reaction zones. Garnet Sm-Nd and Lu-Hf dates range from ca. 115 to 101 Ma (including uncertainties) and correlate with grain size. We interpret the CA-ID-TIMS zircon dates to record the age of magma emplacement and the SHRIMP-RG dates to record a range from igneous crystallization to metamorphic dissolution and reprecipitation and/or local Pb loss. Zircon compositional trends within the garnet reaction zone and host are compatible with locally isolated melt and/or separate intrusive magma batches for the two samples described here. Dates for the largest, ~1 cm, garnet of ~113 Ma record growth during metamorphism, while the smaller grains with younger dates reflect high-temperature intracrystalline diffusion and isotopic closure during cooling. The comprehensive geochronological data set for a single location in the Malaspina Pluton illustrates a complex and protracted geologic history common in granulite facies rocks, estimates lower crustal cooling rates of ~20 °C/m.y., and underlines the importance of multiple chronometers and careful textural characterization for assigning meaningful ages to lower-crustal rocks. Numerous data sets from single locations, like the one described here, are needed to evaluate the spatial extent and variation of cooling rates for Fiordland and other lower crustal exposures.

Keywords: Zircon U-Pb, garnet Sm-Nd, migmatite, lower crust, rates of intrusion, duration of metamorphism

INTRODUCTION AND GEOLOGIC SETTING

Zircon and garnet isotopic dates are widely used for understanding local and orogenic scale processes in magmatic arcs, lower-crustal rocks, and high-grade metamorphic terrains. For example, ages and associated trace-element compositions in zircon are critical components of studies that address magma sources, mixing, and assimilation (e.g., Hammerli et al. 2018). Garnet stability is important for characterizing arc roots because it exerts controls on partial melting processes, the composition of intermediate- to high-silica magmas found in magmatic arcs (e.g., Lee et al. 2006; Ducea et al. 2015), and the density of lower crust and mantle lithosphere (e.g., Kay and Mahlburg Kay 1993). Garnet ages provide a means of understanding processes in magmatic arc roots because they can be directly linked to pressure and temperature estimates for constructing quantitative *P-T-t* paths and calculating rates of tectonic processes (e.g., Stowell et al. 2001, 2007; Lapen et al. 2003; Gatewood et al. 2015). In granulite facies metamorphic rocks, the zircon U-Pb, and garnet Sm-Nd and Lu-Hf ages generally yield significant differences that may reflect igneous, peak metamorphic, and post-peak metamorphic processes (e.g., Mezger et al. 1992; Hoskin and Schaltegger 2003; Harley et al. 2007; Baxter and Scherer 2013; Smit et al. 2013,

---

* E-mail: hstowell@geo.ua.edu
† Orcid 0000-0002-8385-2705

0003-004X/22/0006–1116$05.00/DOI: https://doi.org/10.2138/am-2022-7967

2014; Baxter et al. 2017). For example, Yakymchuk and Brown (2014) used phase equilibria modeling to infer that partially melted granulite may contain multiple generations of zircon, some of which may predate metamorphism and others, which grew during decreasing temperature after the metamorphic peak. The age ranges from each chronometer may be a challenge to interpret, but if interpretation is possible, the results can provide quantitative ages for numerous points in a rock's history. This, in turn, provides the data for calculating heating and cooling rates in the lower crust.

Fiordland is an ideal location for studying lower crustal processes because it is comprised of a mid- to lower-crustal section of a continental magmatic arc that was active along the Gondwana margin from the late Paleozoic (Tulloch et al. 2009; Turnbull et al. 2016) to the Cretaceous (Mattinson et al. 1986; Klepeis et al. 2003; Tulloch and Kimbrough 2003). Fiordland is dominated by paired belts of older mid-crustal plutons on the east (outboard; predominantly Darran suite) and younger lower crustal plutons on the west (inboard; Tulloch and Kimbrough 2003). The western magmatic belt in northern and central Fiordland is dominated by Cretaceous plutons of the Western Fiordland Orthogneiss (WFO). These diorite to monzodiorite plutons intruded between 128 and 114 Ma based on zircon U-Pb geochronology using sensitive high-resolution ion microprobe (SHRIMP) and laser ablation-inductively coupled plasma-mass spectrometry (LA-ICP-MS) analysis (e.g., Hollis et al. 2004; Milan et al. 2016; Schwartz et al. 2017; Decker et al. 2017) and 123 to 117 Ma based on TIMS zircon geochronology (Mattinson et al. 1986; Tulloch and Kimbrough 2003). The Malaspina Pluton is the southernmost of the three largest WFO plutons (Fig. 1) and laser ablation U-Pb zircon ages range from 114 to 117 Ma (e.g., Hollis et al. 2004; Stowell et al. 2014; Milan et al. 2016). Large parts of the WFO, including much of the Malaspina Pluton, were metamorphosed to garnet granulite conditions ca. 112 Ma based on garnet Sm-Nd geochronology (Stowell et al. 2014, 2017). Granulite metamorphism occurred at 12 to 13.5 kbar and temperatures in excess of 850 °C (Oliver 1977, 1980; Bradshaw 1989; Daczko and Halpin 2009; Stowell et al. 2014) after eclogite metamorphism in the Breaksea area (Stowell et al. 2017). Granulite metamorphism locally produced garnet and clinopyroxene mineral assemblages that are commonly associated with leucocratic partial melts. In the WFO, post granulite composite cooling rates of ~50 °C/m.y. (Flowers et al. 2005) and 8–14 °C/m.y. (Schwartz et al. 2016) have been estimated from U-Pb ages and metamorphic temperatures obtained by combining data from multiple sample locations.

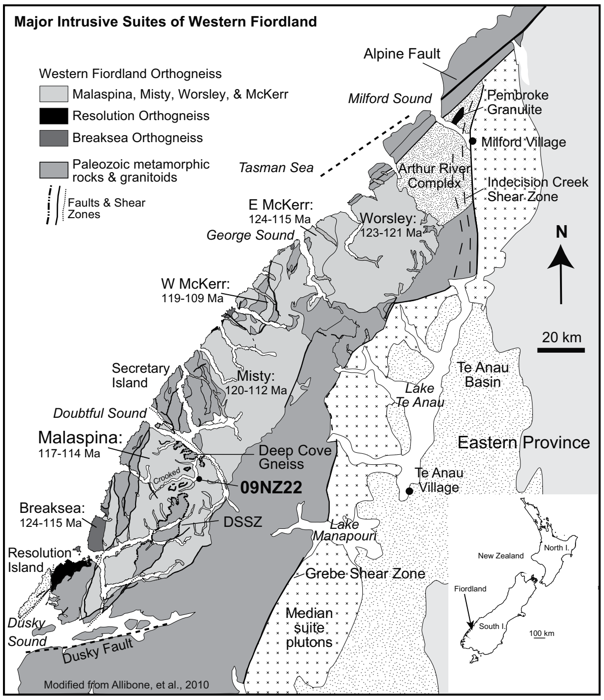

FIGURE 1. Simplified geological map of northern and central Fiordland showing the Western Fiordland Orthogneiss and adjacent rocks, New Zealand. The migmatitic granulite sample 09NZ22 is shown on Crooked Arm. Map inset shows Fiordland along the southwest edge of the South Island New Zealand. Fiordland geology is modified from Allibone et al. (2009) and Turnbull et al. (2010). Worsley = Worsley Pluton; E McKerr = Eastern McKerr Intrusives; W McKerr = Western McKerr Intrusives; Misty = Misty Pluton; Malaspina = Malaspina Pluton; Breaksea = Breaksea Orthogneiss; DSSZ = Doubtful Sound shear zone. Pluton ages are zircon U-Pb results reported in Schwartz et al. (2017).

The mid- to lower- crust of magmatic arcs may have numerous textural occurrences of garnet and some of these are commonly in plutonic rocks (e.g., Stevenson et al. 2005; Hacker et al. 2008; Jagoutz 2010). In plutonic rocks, metamorphic garnet ± clinopyroxene may replace igneous minerals adjacent to cross-cutting and pervasive leucosomes, forming what we refer to here as garnet reaction zones. These garnet reaction zones are widespread in migmatite throughout northern and central Fiordland (e.g., Blattner 1976; Oliver 1977; Clarke et al. 2005; Daczko et al. 2016). The eastern Malaspina Pluton in central Fiordland is partly recrystallized to garnet granulite (Oliver 1980; Turnbull et al. 2010) and lies structurally below the Doubtful Sound shear zone (Fig. 1) (Oliver and Coggon 1979; Gibson and Ireland 1995). This shear zone separates the pluton from dominantly metasedimentary rocks of the overlying Deep Cove Gneiss, and it has been interpreted as an extensional fault by Gibson et al. (1988). The garnet reaction zones in the Malaspina Pluton are centimeters to meters in width and contain dominantly metamorphic mineral assemblages, with largely igneous mineral assemblages and textures outside the garnet reaction zones. The Malaspina Pluton exposed along Crooked Arm (Fig. 1) includes extensive areas of LS tectonites dominated by garnet reaction zones that are cut by 5 to 20 cm wide leucosomes. Locally, leucosome veins have distinct borders of coarse porphyroblasts referred to here as selvages. In the Crooked Arm area these are generally garnet selvages (Fig. 2). Garnet occurrences are classified according to Stowell et al. (2014): Type 1 garnet occurs in discrete garnet reaction zones, Type 2 garnet forms planar to sub-planar arrays as selvages to trondhjemite veins, and Type 3 garnet are porphyroblasts in diffuse leucosomes. Most or all porphyroblastic and selvage garnet must have grown during partial melting based on crystallized melt inclusions and textures (Stowell et al. 2014). Garnet in the garnet reaction zones is directly related to melts and/or fluids and has also been interpreted to have grown during partial melting of the host gneiss (Oliver 1977; Stowell et

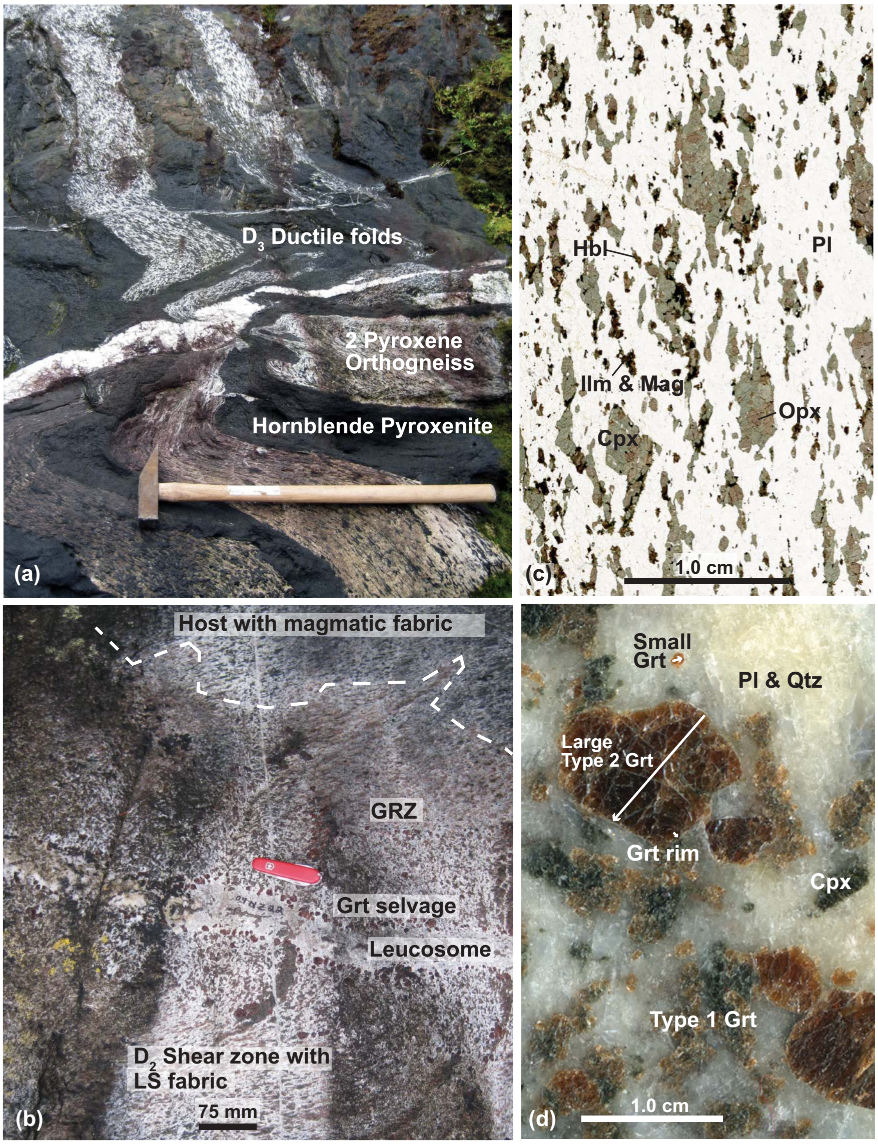

FIGURE 2. Photographs of the Malaspina Pluton along Crooked Arm, New Zealand. (**a**) Ductile folds in diorite gneiss and hornblende pyroxenite layers west of 09NZ22. These folds are tentatively interpreted as D_3. (**b**) Garnet granulite with leucosome vein, which cuts the LS fabric in a wide garnet reaction zone and is bordered by a selvage of 10 to 12 mm euhedral garnet (09NZ22). Leucosome and garnet reaction zone (09NZ22A), and host (09NZ22B) samples discussed here include this vein, garnet selvage, and garnet reaction zone. Fabric correlations are with those from Klepeis et al. (2016). (**c**) Photomicrograph of host orthogneiss in sample 09NZ22b. Note well-developed foliation in this two pyroxene diorite. (**d**) Photograph of the garnet reaction zone in sample 09NZ22a. Type 2 garnet grains form a selvage along the leucosome vein in the upper right. Type 1 garnet are intergrown with clinopyroxene in the lower left part of the photograph. Lines indicate the locations for the EPMA garnet compositions presented in Figure 8 and the arrowheads indicate the right-hand end of the zoning profiles. GRZ = garnet reaction zone. (Color online.)

al. 2014); however, other researchers have inferred that garnet growth in the garnet reaction zones resulted from dehydration of the host rock by externally derived trondhjemite magma (e.g., Clarke et al. 2005).

The outcrops along Crooked Arm are ideal for evaluating the rate of cooling from garnet granulite metamorphic temperatures attained during the development of mylonite fabrics. We present zircon U-Pb, garnet Sm-Nd, and garnet Lu-Hf ages, and trace-element mineral compositions for a single outcrop of the Malaspina Pluton (Figs. 1 and 2). Syn- and post-magmatic strain in much of the pluton (Klepeis et al. 2016), including rocks along Crooked Arm, and metamorphism ca. 4 m.y. after emplacement, produced hornblende pyroxene plagioclase orthogneiss with locally abundant garnet. Much of the orthogneiss is compositionally layered at a 1 to 10 m scale (Fig. 2) with rocks ranging from hornblendite to diorite and monzodiorite. These thick layers are interpreted as igneous in origin. The central part of Crooked Arm is dominated by high-temperature L-S tectonites (Stowell et al. 2014). High-temperature metamorphism with local partial melting at ~920 °C and 14 kbar resulted in diffuse and vein leucosomes that are dominantly trondhjemite in composition (Stowell et al. 2014).

In this contribution, we evaluate zircon and garnet chronometers in granulite facies migmatitic metabasite from Fiordland. The interpretations are based in part on published pressure, temperature, and garnet Sm-Nd age data for metamorphism (Stowell et al. 2014). New data include additional garnet Sm-Nd ages, garnet Lu-Hf ages, new zircon U-Pb ages, and zircon and garnet trace element concentrations. The trace element concentrations and zoning in these minerals provide the context for interpreting the ages. The resulting history of pluton intrusion, high-temperature metamorphism, and partial melting is used to determine the timescales for metamorphism and rates of heating and cooling for a single outcrop along Crooked Arm.

ANALYTICAL METHODS

We compare geochronological data derived from the U-Pb isotopic system in zircon and the Lu-Hf and Sm-Nd isotopic systems in garnet. The zircon U-Pb isotopic data were obtained by secondary ion mass spectrometry (sensitive high-resolution ion microprobe with reverse geometry or SHRIMP-RG) and by chemical abrasion isotope dilution thermal ionization mass spectrometry (CA-ID-TIMS) on single zircon. The garnet isotopic data were obtained from solution multi-collector ICP-MS (Lu and Hf) and ID-TIMS (Sm and Nd).

Mineral compositional analysis

Quantitative major element mineral compositions and mineral zoning maps were obtained from individual point analyses and electron beam rastering, respectively. X-ray maps and quantitative point analyses were obtained on the JEOL 8600 electron probe microanalyzer (EPMA) at the University of Alabama following methods described in Stowell et al. (2010). The $K\alpha$ X-ray maps were obtained using a Bruker energy-dispersive spectrometer and Esprit software. Quantitative point analyses were obtained using wavelength-dispersive spectrometers, CitZAF correction techniques, and Probe for EPMA software (Donovan 2010). Major element data for garnet and other phases was first qualitatively assessed with $K\alpha$ X-ray maps and then quantified as appropriate with point analyses and line scans. Inclusions and compromised analyses were filtered out of the quantitative data. Additional information about EPMA methods and analytical precision at the University of Alabama can be found in Stowell et al. (2010).

Quantitative spot analyses for trace elements in garnet were obtained by LA-ICP-MS. Large garnet trace-element maps were determined by Alan Koenig at the U.S. Geological Survey in Lakewood, Colorado. Analyses were obtained with the CETAC LSX-500 coupled to a Perkin Elmer ELAN DRC-e inductively coupled plasma mass spectrometer (ICP-MS). Instrument operating conditions: wavelength = 266 nm, energy = 9 mJ, spot size = 150 μm, pulse rate 10 s^{-1}, carrier gas = 1.05 L/min Ar, calibration standard = USGS GSE-1g, and 30 s ablation time. Raw intensity data were converted to concentrations using the GeoPro offline data processing package. Calcium, determined by EPMA, was used as an internal standard. Trace-element analyses from small garnet grains were obtained at California State University Northridge. Analyses were obtained with a Teledyne-CETAC Analyte G2 Ar-F_2 excimer LA system attached to a Thermo-Element 2 ICP-MS. Instrument operating conditions: wavelength = 193 nm, energy = 9 mJ, spot size = 40 μm, pulse rate 10 s^{-1}, carrier gas = 1.05 L/min He, calibration standards = USGS BHVO-2g and GSC-1g, and 30 s ablation time. Raw intensity data were converted to concentrations using Iolite offline data processing package (Paton et al. 2011). Calcium, determined by EPMA, was used as an internal standard.

Quantitative spot analyses for trace elements in zircon (Ti, Fe, Y, La, Ce, Nd, Sm, Eu, Gd, Dy, Er, Yb, Hf, U, and Th) were obtained at the Stanford-USGS Micro-Analysis SHRIMP-RG facility. These data were obtained simultaneously from the same analytical volume used for zircon U-Pb isotopic analyses. Trace element zircon standard MAD-1 (Coble et al. 2018) was analyzed at the beginning of the analytical session. Operating conditions were the same as those described below for zircon isotope analysis. Raw intensity data were normalized to count rates for silica (measured as $^{28}Si^{16}O$) and converted to concentrations using SQUID-2 data processing package (Ludwig 2009). A more detailed discussion of these methods, including the standards and analytical precision, are reported in Schwartz et al. (2017).

Zircon isotopic analysis

Approximately 5 kg of fresh rock was collected from two samples from the outcrop shown in Figure 2b for zircon geochronology. Heavy minerals were concentrated out of pulverized rock by sequential use of a Gemini Table, high-density liquid (methylene iodide), and a Frantz magnetic separator. Zircon grains were handpicked under a binocular microscope based on clarity and physical intactness.

Chemical abrasion isotope dilution thermal ionization mass spectrometry (CA-ID-TIMS). Zircon analysis by thermal-ionization mass spectrometry followed the detailed procedures outlined in Ramezani et al. (2011) and involved pre-treatment by a chemical abrasion method modified after Mattinson (2005) to minimize the effects of radioactive decay induced crystal defects and associated Pb-loss. Zircons were heated in a furnace for 60 h at 900 °C. The annealed grains were loaded into FEP polytetrafluoroethylene microcapsules and leached in 29 M HF at 210 °C within a high-pressure vessel for 12 h. The partially dissolved zircon grains were then fluxed in 4 M HNO_3 and 6 M HCl solutions successively on a hot plate and in an ultrasonic bath (1 h each) and rinsed in between with several volumes of ultrapure water. Rinsed zircons were then loaded individually into microcapsules with the EARTHTIME ET535 mixed ^{205}Pb-^{233}U-^{235}U tracer solution (Condon et al. 2015; McLean et al. 2015) and 29 M HF to completely dissolve at 210 °C for 48 h. Pb and U were chemically separated using an HCl-based anion-exchange chemistry after Krogh (1973) and loaded together with a silica gel emitter solution on zone-refined and outgassed rhenium filaments. The Pb and U isotopic compositions were measured on a VG Sector 54 multi-collector thermal ionization mass spectrometer at the Massachusetts Institute of Technology Isotope Laboratory. Pb isotopes were measured by peak-hopping on a Daly photomultiplier ion-counting detector, whereas U isotopes were measured as oxides in a static mode using three Faraday collectors. Correction of isotopic ratios, calculation of dates and propagation of uncertainties were completed using the computer applications Tripoli and ET_Redux (Bowring et al. 2011; McLean et al. 2011). All single-crystal age interpretations are based on $^{206}Pb/^{238}U$ dates, which are reported at 95% confidence level.

SHRIMP-RG. Spot analyses for uranium and lead isotope ratios were obtained at the Stanford-USGS Micro-Analysis SHRIMP-RG facility. Epoxy mounts were gold coated to prevent charging during analysis. Spots were chosen using reflected light and CL images (Fig. 3) based on zonation patterns. Rims and distinct cores were chosen to compare ages. The Temora-2 standard was analyzed after every 3–4 unknown analyses. The Temora-2 analyses during the analytical session were reproducible with a 0.25% distribution about the mean. The O_2^- primary ion beam generated analysis pits ~30 μm in diameter and ~2 μm deep, and sputtered secondary ions were mass analyzed in five cycles through the mass table ($^{28}Si^{16}O$ to $^{238}U^{16}O$) for each sample. Fractionation of Pb relative to Th and U was corrected using the fractionation observed during the analysis of the standard zircon. Common Pb was estimated from the excess ^{207}Pb counts in the measured $^{207}Pb/^{206}Pb$ ratio for each analysis, assuming a Pb isotopic composition from Stacey and Kramers (1975) models for average crustal Pb. Raw data were reduced using SQUID-2 software (Ludwig 2009), and all age calculations and Concordia diagrams were made using IsoplotR (Vermeesch 2018). Analyses with common Pb corrections of >5% were discarded from further consideration. Zircon dates are reported using the common-Pb corrected $^{206}Pb/^{238}U$ age. Individual spot ages and ages discussed in the text are presented with 2σ uncertainties.

Garnet isotopic analyses

Samarium and neodymium isotopes. Methods for Sm-Nd garnet geochronology are modified from those in Stowell et al. (2010, 2014). A full description of the methods is available online (https://radis.as.ua.edu/radis-and-isopet-procedures/). Garnet and clinopyroxene were separated from the garnet reaction zone by crushing a section of rock containing only <2 mm garnet grains and then handpicking. These grains were crushed using a carbide steel mortar and pestle and then manually picked under a binocular microscope to avoid mineral inclusions. Additional inclusions were removed by leaching garnet with HF and $HClO_4$ acids (e.g., Gatewood et al. 2015). Whole rock and matrix were prepared from ~1 cm cubes of cut rock and the matrix was separated by crushing and removing all garnet from one of the cubes. All samples were then fully dissolved with HF and nitric acids in SAVILLEX PFA vials on a hot plate. Sample aliquots were spiked with mixed Sm and Nd Spike B from the University of North Carolina at Chapel Hill. REE fractions were separated and concentrated from samples using disposable polyprep BioRad ion chromatography columns. Samarium and Nd splits were separated from the REE fractions using methylactic acid (MLA) and custom-designed 23 cm silica glass columns. Samarium isotopes were measured as metal and Nd isotopes measured as oxide using the VG Sector 54 Thermal Ionization Mass Spectrometer (TIMS) in the Radiogenic Isotope Laboratory (RadIs) at the University of Alabama. Neodymium isotope ratios were normalized to ^{146}Nd/^{144}Nd = 0.7219 and then used with Sm isotope values to compute final isotope ratios and elemental concentrations by isotope dilution. The JNdi Nd standard was run as an oxide periodically during data collection, and the results were ^{143}Nd/^{144}Nd = 0.512117 ± 0.000013 as compared to ^{143}Nd/^{144}Nd = 0.512115 ± 0.000007 reported by Tanaka et al. (2000); therefore, no additional Nd isotope normalization was required. The Sm-Nd isochrons were regressed using the decay constant of 6.540×10^{-12} y^{-1} for λ^{147}Sm (Lugmair and Marti 1978; Begemann and others 2001). Sm-Nd isochrons were calculated and plotted with IsoplotR (Vermeesch 2018). The Sm-Nd age for ~1 cm garnet in Stowell et al. (2014), originally calculated using Isoplot (Ludwig 2012) was recalculated for this study using IsoplotR, resulting in a 0.3 Ma age increase.

Lutetium and hafnium isotopes. Garnet separates and two whole-rock powders—one digested in a hydrothermal vessel and one digested on a hot plate—were analyzed for Lu-Hf geochronology. The Lu and Hf isotope ratios were determined on a Thermo-Scientific Neptune MC–ICP-MS in the Radiogenic Isotope and Geochronology Laboratory at Washington State University. The detailed procedures for sample digestion, spiking, isotope analyses, and data reduction are described in Vervoort et al. (2004) and Cheng et al. (2008). Hafnium isotopic compositions were corrected for mass fractionation with an exponential law using ^{179}Hf/^{177}Hf = 0.7325 and normalized, over the course of this work, relative to ^{176}Hf/^{177}Hf = 0.282160 for the JMC475 Hf standard. External uncertainties applied to measured data for the purpose of data regressions and age calculations are 0.5% for ^{176}Lu/^{177}Hf, and a combination of 2σ in-run error and a blanket 0.005% uncertainty added in quadrature for ^{176}Hf/^{177}Hf. The Lu–Hf isochrons were regressed using the decay constant of 1.867×10^{-11} y^{-1} for λ^{176}Lu (Scherer et al. 2001; Söderlund et al. 2004). Lu and Hf isochrons were calculated and plotted with IsoplotR (Vermeesch 2018).

RESULTS

Sampling for this study focused on the host pluton containing orthopyroxene, clinopyroxene, hornblende, and plagioclase; a garnet reaction zone containing clinopyroxene, garnet, and plagioclase; and garnet selvages along cross-cutting trondhjemite veins. Approximately 1 cm garnets in the vein selvages (Type 2) are arranged in a planar fashion that typically comprises a narrow array on both sides of the trondhjemite leucosomes (Fig. 2). Smaller, 0.05 to 0.2 cm garnets are restricted to the garnet reaction zones (Type 1) and form monomineralic lenses and intergrowths with clinopyroxene. Garnet in the selvages contains numerous rutile inclusions, some of which are crystallographically aligned, and lesser abundances of clinopyroxene, apatite, titanite, ilmenite, zircon, spinel, and plagioclase inclusions. Rare polyphase inclusions of albite, potassium feldspar, and quartz in garnet are interpreted as trapped melts. In this interpretation, these granitic melts approximate the initial melt composition prior to crystallization, fractionation, and melt movement along the vein.

Zircon morphology and cathodoluminescence

Zircon is abundant in the host monzodiorite gneiss and in garnet reaction zones adjacent to trondhjemite veins. Zircons in the host rock are 100 to 300 μm, rounded, anhedral, and embayed grains that are characterized by sector, patchy, and locally faint oscillatory zoning (Figs. 3 and 4). Host zircon grains lack identifiable outer zones (i.e., rims) that can be readily analyzed with a laser or ion beam. Zircons in the garnet reaction zone are 100 to 300 μm and vary from subhedral prismatic to anhedral with numerous embayments (Figs. 3 and 4). The CL images show patchy zoning, luminescent rims (Fig. 3), and a lack of coherent oscillatory or sector zoning. A few garnet reaction zone zircons have identifiable outer zones from later growth (Fig. 3). These narrow rims were targeted with the SHRIMP-RG ion beam.

Zircon U-Pb CA-ID-TIMS ages. Five zircon grains from the garnet reaction zone and five zircon grains from the host pluton were analyzed by CA-ID-TIMS (Table 1; Fig. 4). The analyses from both samples display (geologic) scatter in excess of analytical uncertainty and do not define single age populations.

Zircon from the host orthogneiss (09NZ22b) range in ^{206}Pb/^{238}U age from 118.30 ± 0.13 to 116.70 ± 0.12 Ma. The garnet reaction zone zircon (09NZ22a) range in ^{206}Pb/^{238}U age from 117.65 ± 0.25

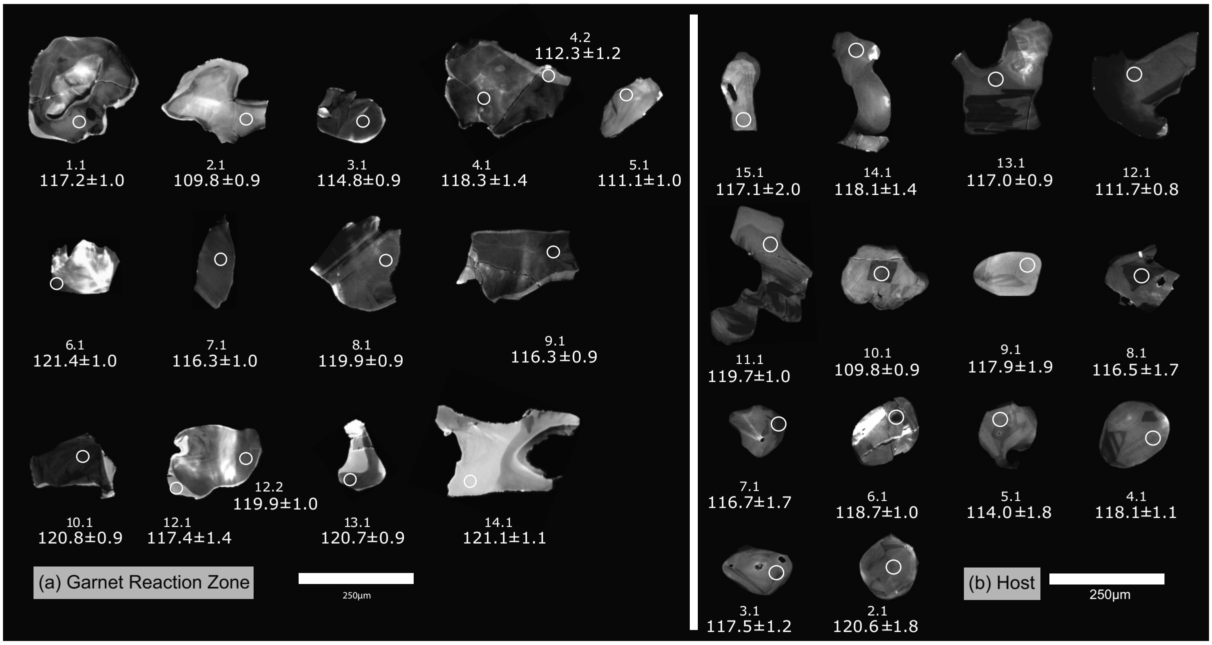

FIGURE 3. Cathodoluminescence images of zircon from migmatite in 09NZ22, Crooked Arm New Zealand. (**a**) Zircon from orthogneiss host, 09NZ22b. (**b**) Zircon from garnet reaction zone adjacent to trondhjemite vein, 09NZ22a. Circles indicate position of SHRIMP-RG U-Pb analyses, top number is grain and analysis number, and bottom number is age and 2σ uncertainty in Ma. (Color online.)

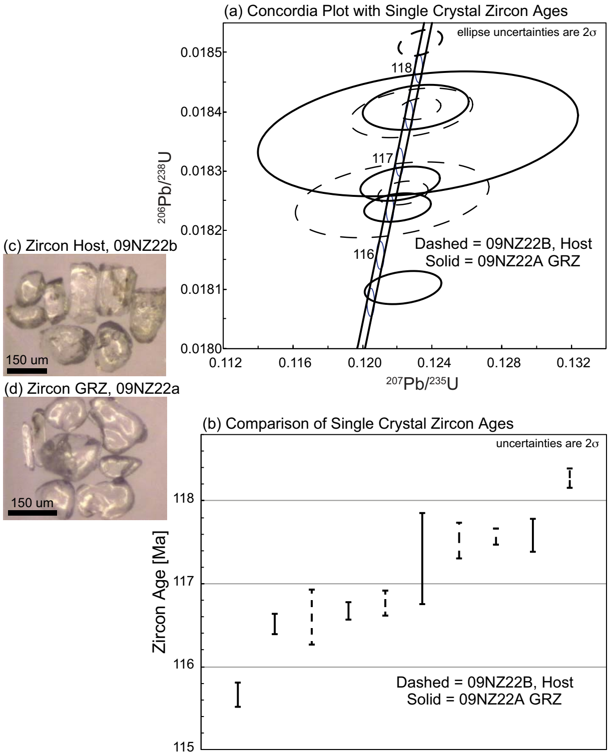

FIGURE 4. U-Pb CA-ID-TIMS ages determined for chemically annealed zircon from 09NZ22 migmatite, Crooked Arm New Zealand. (**a**) Concordia plot showing the error-weighted ellipses for zircon from host (dashed lines) and garnet reaction zone (solid lines). (**b**) Comparison of the ^{238}U-^{206}Pb zircon ages for the same data shown in (**a**). Note the significant overlap between host and GRZ zircon ages and the single outlier at 115.70 Ma. (**c**) Photograph of host zircon grains analyzed by CA-ID-TIMS. (**d**) Photograph of garnet reaction zone zircon grains analyzed by CA-ID-TIMS. (Color online.)

to 115.70 ± 0.18 Ma. The ca. 118.3 to 116.7 Ma ages reported here overlap within uncertainty with the calculated weighted mean ^{206}Pb/^{238}U date of the younger zircon populations (117.5 ± 1.0 Ma) for the Malaspina Pluton at First Arm based on SHRIMP-RG U-Pb geochronology (Schwartz et al. 2017), and are consistent with an ID-TIMS age (multigrain zircon) of 116.6 ± 1.2 Ma from Wet Jacket Arm (Fig. 1) (Mattinson et al. 1986; Tulloch and Kimbrough 2003). See Online Materials[1] Table OM1 for more information.

Zircon U-Pb SHRIMP-RG ages. Fifteen zircon grains from the garnet reaction zone sample 09NZ22a and 14 zircon grains from the host rock sample 09NZ22b were analyzed using the SHRIMP-RG (Table 2). Individual ^{206}Pb/^{238}U ages for these samples range from 121.4 ± 2.0 to 109.8 ± 1.8 Ma. CL images do not indicate distinctive zircon cores; however, narrow rims were identified on a few garnet reaction zones grains (Fig. 3). Three zircon rims targeted via CL images (Fig. 3) yielded ^{206}Pb/^{238}U ages of 112.3 ± 2.4 (GRZ-4.2), 117.4 ± 2.6 and 121.4 ± 2.0 Ma (GRZ-6.1): together these three ages are indistinguishable from the overall age population. However, a single pair of garnet reaction zone analyses (Fig. 3, analyses 4.1 and 4.2) yield a statistically significant and logical age progressive core (118.3 ± 2.7) and rim (112.3 ± 2.4) ages. Young rims were either absent from the host orthogneiss zircon or too narrow for the ion beam spot size to be analyzed (Fig. 3). However, the range of ages for these host zircons (109.8 to 120.6) is indistinguishable from the range of ages (109.8 to 121.4) for garnet reaction zone zircon.

The garnet reaction zone SHRIMP-RG zircon ages are over-dispersed, and the weighted mean age of 117.1 ± 2.0 Ma has an MSWD of 15.5 (no ages rejected), indicating that these ages do not consist of a single meaningful population. Rejection of the six youngest ages, which form a stair-step array to lower ages, results in a weighted mean age of 119.8 ± 1.2 Ma (Fig. 5) with an MSWD of 2.3. Similarly, the host SHRIMP-RG zircon ages are over-dispersed and the weighted mean age of 116.0 ± 2.0 Ma has an MSWD of 9.2 (no ages rejected). Rejection of the two youngest ages results in a weighted mean age of 117.9 ± 0.9 Ma (Fig. 5) with an MSWD of 1.3. This 117.9 Ma age determined for the host (09NZ22b) from Crooked Arm is indistinguishable from the weighted mean for the garnet reaction zone zircon. The young zircon ages, rejected from the weighted means for the host and garnet reaction zone overlap with garnet Sm-Nd ages for this sample and others from the Malaspina Pluton (Stowell et al. 2014), and metamorphic zircon and titanite in the region (Schwartz et al. 2016).

Garnet ages

New Sm and Nd isotope data for 0.5 to 2 mm diameter garnet grains, clinopyroxene, matrix, and whole-rock from Type 1 garnet reaction zone garnet (09NZ22) define a 5-point isochron with an age of 103.6 ± 2.2 Ma (Table 3; Fig. 6). An additional single garnet aliquot combined with the clinopyroxene, whole rock, and matrix results in a 4-point isochron age of 112.1 ± 2.4 Ma indistinguishable from the published age of 112.8 ± 2.2 Ma (Stowell et al. 2014) and the recalculated age of 113.1 Ma (Table 3) for ~1 cm garnet in this sample.

One core and six rims from the ~11 mm Type 2 garnet grains and two whole-rock aliquots were analyzed for garnet Lu-Hf geochronology (Table 3). The whole rock aliquots have notably dissimilar ^{176}Hf/^{177}Hf values, one of which falls well below the isochron for the remaining garnet and rock (Fig. 6). The whole rock aliquot dissolved in a PFA vial has a dramatically lower ^{176}Lu/^{177}Hf ratio of 0.015739 compared to the aliquot dissolved in a hydrothermal vessel with ^{176}Lu/^{177}Hf = 0.016119. We exclude the aliquot dissolved in PFA (WR S1 – PFA) because it may not have completely dissolved and inclusion of these isotope ratios produce an age ca. 124 Ma, which is significantly older than U-Pb zircon ages for this sample and the pluton emplacement age determined from multiple samples (Schwartz et al. 2017). The remaining eight aliquots result in an age of 111.2 ± 1.2 Ma (MSWD = 0.98). The whole-rock isotopic compositions may have been modified by partial melting and/or biased by igneous zircon that was not in equilibrium with garnet. Excluding both whole-rock isotope values resulted in an age of 114.8 ± 3.5 Ma (MSWD = 0.25) for the seven garnet aliquots. Both of these younger ages overlap within the uncertainty of the ~1 cm garnet Sm-Nd results [Table 4 and Stowell et al. (2014)].

Major and trace element compositions of zircon and garnet

Trace-element concentrations were obtained for the 29 zircon spots that were analyzed simultaneously with U and Pb isotopes

TABLE 1. U-Pb isotopic data for CA-ID-TIMS zircon analyses from the Malaspina Pluton, Crooked Arm, New Zealand

					Ratios								Ages (Ma)						
Sample Fractions (a)	Pb(c) (pg) (b)	Pb*/ Pb(c) (b)	U (pg) (c)	Th/ U	^{206}Pb/ ^{204}Pb (d)	^{208}Pb/ ^{206}Pb (e)	^{206}Pb/ ^{238}U (f)	err (2σ%)	^{207}Pb/ ^{235}U (f)	err (2σ%)	^{207}Pb/ ^{206}Pb (f)	err (2σ%)	^{206}Pb/ ^{238}U	err (2σ)	^{207}Pb/ ^{235}U	err (2σ)	^{207}Pb/ ^{206}Pb	err (2σ)	corr. coef.
Sample 09NZ22B: Host orthogneiss																			
z5	0.54	23.5	604	0.84	1302.5	0.268	0.018520	(.11)	0.12344	(1.03)	0.04836	(.99)	118.30	0.13	118.2	1.2	116	23	0.40
z4	0.53	21.3	557	0.76	1203.6	0.241	0.018409	(.10)	0.12339	(1.05)	0.04863	(1.02)	117.59	0.11	118.1	1.2	129	24	0.35
z3	0.54	9.1	233	0.89	510.9	0.284	0.018408	(.23)	0.12308	(2.83)	0.04852	(2.76)	117.59	0.26	117.9	3.2	123	65	0.38
z1	0.80	5.5	197	1.19	296.6	0.379	0.018269	(.37)	0.12220	(4.67)	0.04853	(4.54)	116.71	0.43	117.1	5.2	124	107	0.38
z2	0.63	21.6	613	1.16	1113.8	0.368	0.018267	(.11)	0.12246	(1.20)	0.04864	(1.17)	116.70	0.12	117.3	1.3	130	27	0.33
Sample 09NZ22A: Garnet reaction zone																			
z2	0.54	8.8	234	0.75	510.2	0.240	0.018417	(.21)	0.12334	(2.57)	0.04859	(2.51)	117.65	0.25	118.1	2.9	127	59	0.33
z1	0.59	2.8	84	0.66	178.4	0.211	0.018394	(.62)	0.12405	(7.76)	0.04894	(7.56)	117.50	0.72	118.7	8.7	144	177	0.36
z3	1.19	11.8	724	0.58	703.9	0.183	0.018286	(.16)	0.12237	(1.91)	0.04856	(1.85)	116.81	0.18	117.2	2.1	125	44	0.37
z4	0.55	12.9	369	0.58	769.9	0.184	0.018245	(.14)	0.12220	(1.65)	0.04860	(1.61)	116.55	0.16	117.1	1.8	127	38	0.33
z5	1.64	11.2	949	0.60	664.8	0.191	0.018111	(.16)	0.12254	(1.90)	0.04910	(1.85)	115.70	0.18	117.4	2.1	151	43	0.34

Notes: (a) Thermally annealed and pre-treated single zircon. (b) Total common-Pb in analyses. Pb* is radiogenic Pb content. (c) Total sample U content. (d) Measured ratio corrected for spike and fractionation only. (e) Radiogenic Pb ratio. (f) Corrected for fractionation, spike, and blank. Also corrected for initial Th/U disequilibrium using radiogenic ^{208}Pb and Th/U$_{magma}$ = 2.8. Mass fractionation correction of 0.25%/amu ± 0.04%/amu (atomic mass unit) was applied to single-collector Daly analyses. All common Pb assumed to be laboratory blank. Total procedural blank less than 0.1 pg for U. Blank isotopic composition: ^{206}Pb/^{204}Pb = 18.15 ± 0.47, ^{207}Pb/^{204}Pb = 15.30 ± 0.30, ^{208}Pb/^{204}Pb = 37.11 ± 0.87. Corr. coef. = correlation coefficient. Ages calculated using the decay constants λ_{238} = 1.55125E-10 y^{-1} and λ_{235} = 9.8485E-10 y^{-1} (Jaffey et al. 1971).

TABLE 2. Zircon U-Pb isotope data, SHRIMP-RG from the Malaspina Pluton, Crooked Arm, New Zealand

	Concentrations				Atomic ratios[a]						Age (Ma)			Weighted mean age	
Zrn grain	Ti (ppm)	U (ppm)	^{232}Th/ ^{238}U	^{206}Pb[b] (ppm)	^{238}U/ ^{206}Pb[c]	% err ± (1σ)	^{207}Pb/ ^{206}Pb[d]	% err ± (1σ)	^{206}Pb/ ^{238}U[e]	% err ± (1σ)	*T* (°C) (Ti-Zrn)	^{206}Pb/ ^{238}U[f]	err abs ± (2σ)	Age (Ma) ± (2σ)	
GRZ															
GRZ-2.1	15	165	1.29	2.4	58.18	0.80	0.0490	5.1	0.01722	1.42	862	*109.8*	*1.8*		
GRZ-5.1	18	142	0.52	2.1	57.66	0.83	0.0465	5.7	0.01757	1.30	885	*111.1*	*1.9*		
GRZ-4.2	33	120	0.67	1.8	57.22	0.91	0.0442	10.5	0.01735	1.60	956	*112.3*	*2.4*		
GRZ-3.1	26	226	0.49	3.5	55.68	0.73	0.0477	4.4	0.01798	1.00	925	*114.8*	*1.7*		
GRZ-9.1	13	261	0.58	4.1	54.98	0.70	0.0479	4.0	0.01821	0.87	850	*116.3*	*1.7*		
GRZ-7.1	16	158	0.54	2.5	54.60	0.81	0.0534	4.8	0.01835	1.15	873	*116.3*	*2.0*		
GRZ-1.1	14	185	0.71	2.9	54.72	0.77	0.0450	4.9	0.01820	1.04	858	117.2	1.9	119.8 ± 1.2	9/15 pts.
GRZ-12.1	24	96	0.88	1.5	54.53	1.09	0.0465	6.8	0.01807	1.91	918	117.4	2.6		
GRZ-4.1	16	277	0.56	4.4	54.16	1.14	0.0462	3.9	0.01852	1.22	870	118.3	2.7		
GRZ-8.1	23	234	0.48	3.8	53.32	0.72	0.0478	4.1	0.01882	0.92	910	119.9	1.8		
GRZ-12.2	27	223	0.46	3.6	53.07	0.78	0.0515	4.1	0.01873	1.05	929	119.9	1.9		
GRZ-13.1	30	238	0.47	3.9	52.97	0.71	0.0474	4.1	0.01894	0.85	946	120.7	1.8		
GRZ-10.1	16	265	0.56	4.3	53.00	0.70	0.0464	3.9	0.01885	0.91	870	120.8	1.7		
GRZ-14.1	27	123	0.52	2.0	52.83	0.88	0.0471	5.7	0.01904	1.27	931	121.1	2.2		
GRZ-6.1	32	177	0.49	2.9	52.50	0.78	0.0500	4.5	0.01907	1.16	953	121.4	2.0		
Host															
Host-10.1	14	278	1.05	4.1	58.11	0.71	0.0492	7.2	0.01719	0.88	855	*109.8*	*1.8*		
Host-12.1	26	278	0.44	4.2	57.17	0.69	0.0491	3.9	0.01734	0.95	927	*111.7*	*1.6*		
Host-5.1	25	156	0.87	2.4	56.01	1.51	0.0487	5.1	0.01776	1.91	922	114.0	3.4	117.9 ± 0.9	12/14 pts.
Host-8.1	15	222	0.90	3.5	54.83	1.44	0.0486	4.3	0.01835	1.56	860	116.5	3.3		
Host-7.1	36	192	0.81	3.0	54.68	1.42	0.0493	4.5	0.01817	1.66	968	116.7	3.3		
Host-13.1	36	225	0.47	3.5	54.49	0.73	0.0498	4.2	0.01833	0.90	968	117.0	1.8		
Host-15.1	13	138	0.79	2.2	54.45	1.71	0.0496	5.3	0.01826	1.94	845	117.1	4.0		
Host-3.1	42	190	0.93	3.0	54.15	0.83	0.0515	8.8	0.01833	1.20	988	117.5	2.3		
Host-9.1	18	153	0.88	2.4	54.14	1.62	0.0489	5.1	0.01838	1.94	882	117.9	3.8		
Host-14.1	35	218	0.46	3.5	54.08	1.15	0.0487	4.2	0.01838	1.35	963	118.1	2.7		
Host-4.1	16	145	0.89	2.3	54.05	0.83	0.0487	5.3	0.01847	1.37	869	118.1	2.1		
Host-6.1	30	173	0.92	2.8	53.69	0.79	0.0498	4.8	0.01854	1.07	942	118.7	1.9		
Host-11.1	35	238	0.47	3.8	53.99	0.77	0.0392	4.6	0.01862	1.16	964	119.7	1.9		
Host-2.1	49	147	0.85	2.4	52.75	1.42	0.0516	5.0	0.01866	1.77	1009	120.6	3.4		

[a] Errors are percentages reported at 1σ level.

[b] Radiogenic ^{206}Pb.

[c] Fraction of total ^{206}Pb that is common ^{206}Pb.

[d] Uncorrected ratios.

[e] ^{207}Pb corrected ratios using age-appropriate Pb isotopic composition of Stacey and Kramers (1975).

[f] ^{207}Pb corrected age. Spot analyses in italic were used to calculate the weighted average for the young age population.

using the SHRIMP-RG (Fig. 7). The major and trace element zoning in Type 1 and 2 garnet were characterized with lines of wavelength dispersive point analyses (Fig. 8). In addition, new laser ablation inductively coupled mass spectrometer (LA-ICP-MS) trace element data are presented for small garnet grains and a subset of analyses reported in Stowell et al. (2014) for ~1 cm garnet grains are presented here.

Zircon from the host and garnet reaction zone is distinguished by contrasting trace-element concentrations and magma evolution trends (Figs. 7a–7h). For example, host zircons have both higher average and a more extended range in Hf concentrations (Figs. 7a–7f) than the garnet reaction zone zircon. We observe

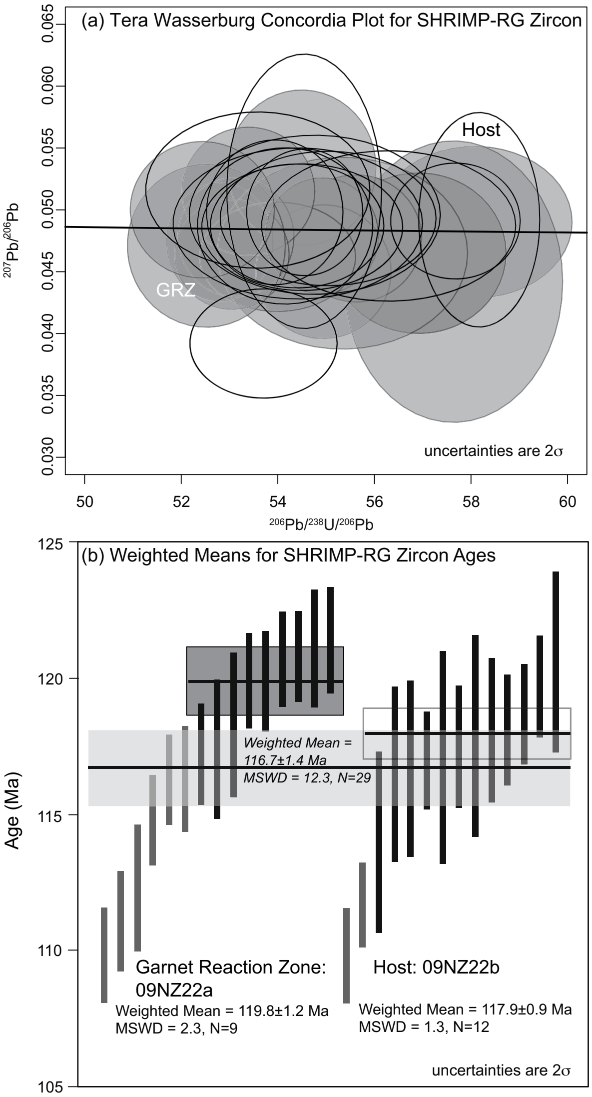

FIGURE 5. U-Pb ages determined from SHRIMP-RG analysis of zircon from 09NZ22 migmatite, Crooked Arm New Zealand. (**a**) Tera Wasserburg concordia plot showing error ellipses and spread of ages along concordia. All but one of the host ages are concordant within uncertainty. (**b**) All the 29 ^{238}U-^{206}Pb zircon ages shown in (**a**) have a weighted mean age of 116.7 ± 1.4 Ma with an MSWD of 12.3. Separation of the ages into garnet reaction zone and Host also produces weighted mean ages with high MSWD; however, exclusion of the youngest ages from each data set results in weighted mean ages that overlap at 2σ uncertainties and have MSWD values <2.5: GRZ = 119.8 ± 1.2 and Host = 117.9 ± 0.9 Ma. The 8 younger ages, shown in gray extend down to and overlap with garnet ages and are interpreted to result from Pb loss.

TABLE 3. Garnet Sm-Nd and Lu-Hf isotope data from the Malaspina Pluton, Crooked Arm, New Zealand

Sample	$[\mathrm{Sm}]_{ppm}$	$[\mathrm{Nd}]_{ppm}$	^{147}Sm/^{144}Nd	2 SE	^{143}Nd/^{144}Nd	2 SE	Age (Ma) (± 2σ)		Sample	$[\mathrm{Lu}]_{ppm}$	$[\mathrm{Hf}]_{ppm}$	^{176}Lu/^{177}Hf	2s (Abs)	^{176}Hf/^{177}Hf	2s (Abs)	Age (Ma) (±2σ)	
09NZ22a (P82421): 1 cm grain (Stowell et al. 2014)							113.1 ± 2.2[a]	10 pt	09NZ22a (P82421):							111.2 ± 1.2	8 pt
09NZ22A-GRZ: 0.5–2 mm diameter grains							103.6 ± 2.2[b]	5 pt	WR B1	0.099	0.873	0.016119	0.000081	0.282971	0.000015		
WR	4.32	20.15	0.1296	0.0009	0.512651	0.000008			*WR S1*	*0.093*	*0.839*	*0.015739*	*0.000079*	*0.282475*	*0.000020*		
Mtx	1.46	8.99	0.0982	0.0007	0.512619	0.000008			Grt 2 Rim1 G2	2.509	0.475	0.749444	0.003747	0.284489	0.000015	114.8 ± 3.5	7 pt
Cpx	8.74	37.93	0.1394	0.0010	0.512647	0.000009			Grt 2 Rim2 G3	2.506	0.532	0.668555	0.003343	0.284316	0.000015		
									Grt 2 Rim3 G4	3.049	0.511	0.846090	0.004230	0.284696	0.000015		
									Grt 2 Core2 G9	3.036	0.510	0.845221	0.004226	0.284702	0.000015		
GX	3.78	3.28	0.6958	0.0049	0.513024	0.000008			Grt 2 Rim1 2 G10	1.947	0.462	0.598138	0.002991	0.284163	0.000016		
GXfb	3.20	2.66	0.7262	0.0051	0.513055	0.000012			Grt 2 Rim2 2 G11	2.107	0.499	0.599703	0.002999	0.284176	0.000016		
							112.1±2.4[c]	4 pt	Grt 2 Rim3 2 G12	2.390	0.500	0.678888	0.003394	0.284341	0.000016		
GXfa	3.95	3.22	0.7427	0.0052	0.513094	0.000008											

Notes: Italic data are excluded from age calculations. Grt = garnet; Cpx = clinopyroxene; WR = whole rock (B = vessel dissolution, S = Savillex vial); Mtx = rock minus garnet.

[a] Recalculated using IsoplotR. [b] GX and GXfb are multigrain aliquots used with WR, Mtx, and Cpx for age calculation. [c] GXfa was used with WR, Mtx, and Cpx for age calculation.

no apparent correlation between Hf (ppm) and SHRIMP-RG age, though large errors on individual spots (3–4 m.y., 2σ) preclude the use of SHRIMP-RG data for interpreting fine-scale details of magma evolution (inset Fig. 7a). Garnet reaction zone zircons also have lower overall middle and heavy REE concentrations compared to host zircons and show little to no increase in REE concentrations with increasing Hf (ppm) and magma differentiation (Figs. 7a–7c). In contrast, host zircons show a strong increase in middle and heavy REE concentrations during differentiation (Figs. 7a, 7b, 7c, and 7g). Neither garnet reaction zone nor host zircon shows a strong depletion in HREEs in chondrite-normalized REE abundance plots (Fig. 7h).

All zircon grains have positive Ce anomalies and small negative Eu anomalies; however, host and garnet reaction zone zircon show distinct magmatic trends in Ce/Ce* and Eu/Eu*. The contrasting initial Ce/Ce* values shown in Figure 7d suggest different feldspar fractionation or initial magmatic oxidation states (Trail 2012). In addition, garnet reaction zone zircons have less pronounced Eu/Eu*, a measure of the magnitude of the Eu anomaly, compared to host zircons (Fig. 7e). The latter is consistent with the more extended range in Hf (ppm). Zircon in the garnet reaction zone and host also show increasing Th/U with differentiation, but the trends are distinct (Figs. 7f and 7g). Initial Th/U values converge at Th/U = 0.4, and then show contrasting trends. Thus, although the cross-cutting relations and garnet ages indicate that the garnet reaction zone and veins are younger, the unique trace element characteristics and trends observed in the garnet reaction zone zircon indicate that they are not logically interpreted as late products of a crystallization trend in a single simple magma, and the two samples cannot be related by simple partial melting or fractionation processes.

The Ti content of zircon (SHRIMP-RG) from host and garnet reaction zone in 09NZ22 ranges from 13 to 49 ppm. These Ti contents are used to estimate zircon growth temperatures using the thermometer of Ferry and Watson (2007), assuming activities of 0.8 for Si and 0.7 for Ti, and the pressure correction described in Ferriss et al. (2008). These activities are reasonable for the host rock because it does not contain quartz and rutile, and these values result in calculated temperatures that match those estimated for amphibole crystallization in the Malaspina Pluton (Carty et al. 2021). However, quartz occurs as small inclusions within Type 2 selvage garnet in the garnet reaction zone and is predicted to be stable near the solidus (Stowell et al. 2014). The activity of Ti was likely to have been less than that of saturation based on the general lack of rutile in the matrix of host and garnet reaction zone samples. However, rutile inclusions in garnet and the prediction of rutile stability in pseudosections (Stowell et al. 2014) indicate that Ti activity was higher, at least during the latter part of metamorphism. Although some zircon may have grown and/or equilibrated during metamorphism, most zircon ages and chemical compositions are compatible with growth during the initial crystallization of the pluton, so we utilize the activities compatible with initial igneous crystallization. Uncertainties in the Ti-in-zircon temperatures are likely to be ca. 60 °C as given by Ferry and Watson (2007) because the activities of SiO_2 and TiO_2 are reasonably well constrained for the Malaspina Pluton samples. The Ti in zircon temperature estimates range from 980 °C down to 822 °C (Table 2); however, the lowest *T* estimates cannot be clearly correlated with zircon rims that have obvious CL overgrowths. This range in temperature extends from above to slightly below those predicted from garnet compositions (Stowell et al. 2014). Temperatures calculated from Ti-in-zircon were plotted with the corresponding U-Pb ages for each grain (Fig. 9). Results show two scattered trends toward lower temperature estimates with younger ages.

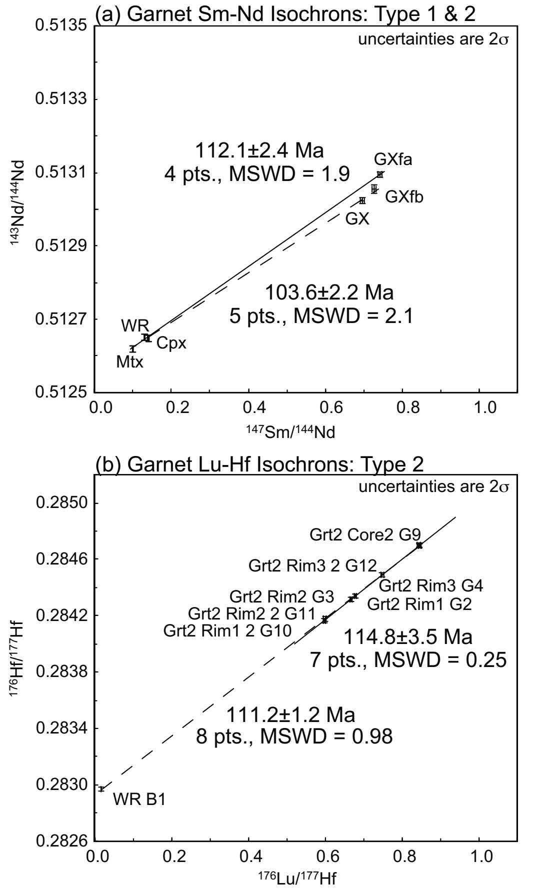

FIGURE 6. Sm-Nd and Lu-Hf isochron ages for garnet reaction zones in migmatite from Crooked Arm New Zealand. (**a**) Garnet and whole rock Sm and Nd isotope results. Note the ca. 8 m.y. difference between the age for a single aliquot at ca. 112 Ma (solid line) and the other aliquots at ca. 104 Ma (dashed line). The 112 Ma age is within uncertainty of the age for large garnet ca. 113 Ma in this sample (Stowell et al. 2014). (**b**) Garnet and whole rock Lu and Hf isotope results. Note the large difference between the isochron for seven garnet fractions ca. 115 Ma (solid line) and for seven garnet fractions with whole rock ca. 111 Ma (dashed).

Large, ~10 mm garnet from Crooked Arm display complex zoning in trace elements (Stowell et al. 2014). These Type 2 garnet grains from the vein selvage have concentric oscillatory zoning in the heavy REE and little or no zoning in the light REE. The oscillations in heavy REE are superposed on broad decreases in concentrations from core to rim (Fig. 8). Samarium is weakly zoned with small-scale oscillations and a general decrease from core to rim. Chondrite-normalized REE patterns have steep positive slopes from La to Eu and near-horizontal HREE segments (Fig. 8). Similarly, to the zircon, there is no clear evidence for equilibrium between the ~10 mm garnet grains and zircon. Large garnets have low-amplitude oscillations in Hf concentrations. Small Type 1 garnet grains from the garnet reaction zone in 09NZ22 have relatively simple zoning (Fig. 8). These grains have no systematic zoning in Nd, although a few spurious points near the rim of garnet suggest possible Nd variation or Nd-bearing

TABLE 4. Sm-Nd closure temperature estimates for garnet from the Malaspina Pluton, Crooked Arm, New Zealand

Sample	Cooling rate (C/m.y.)	Garnet radius mm	Diffusion parameters	Closure *T* (°C)	Diffusion parameters	Closure *T* (°C)
09NZ22a (P82421)			D(m^2/s) Nd[a]		D(m^2/s) Nd[b]	
	–15	0.5–1.0	1.21E-20	690–740	3.00E-22	865–915
	–20	0.5–1.0		700–750		870–920
	–25	0.5–1.0		710–760		875–930
	–15	6		885		1060
	–20	6		900		1070
	–25	6		910		1080

[a] From Bloch et al. (2020).

[b] From Carlson (2012).

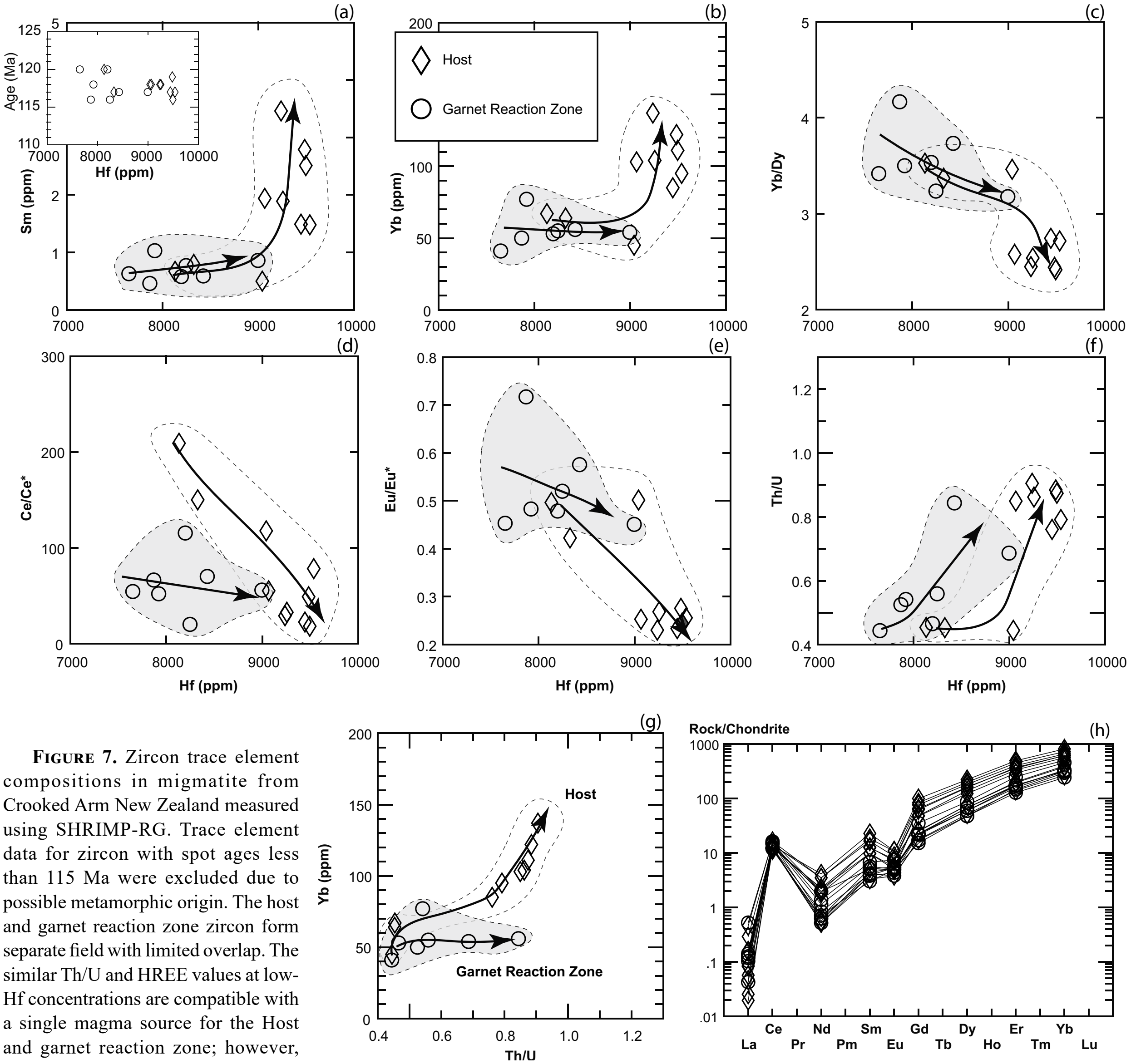

FIGURE 7. Zircon trace element compositions in migmatite from Crooked Arm New Zealand measured using SHRIMP-RG. Trace element data for zircon with spot ages less than 115 Ma were excluded due to possible metamorphic origin. The host and garnet reaction zone zircon form separate field with limited overlap. The similar Th/U and HREE values at low-Hf concentrations are compatible with a single magma source for the Host and garnet reaction zone; however, trends indicate significantly greater fractionation for host rock. (**a**) Sm vs. Hf in zircon. Inset shows the lack of a trend in U-Pb zircon age vs. Hf. (**b**) Yb vs. Hf in zircon. (**c**) Yb/Dy vs. Hf in zircon. (**d**) Ce/Ce* vs. Hf in zircon. Ce* = Ce predicted from slope of line between adjacent REE. (**e**) Eu/Eu* vs. Hf in zircon. Eu* = Eu predicted from slope of line between adjacent REE. (**f**) Th/U vs. Hf in zircon. (**g**) Yb vs. Th/U in zircon. (**h**) Chondrite-normalized REE values for zircon. Steep curves for Host and garnet reaction zone indicate that zircon was not in equilibrium with garnet during growth. Chondrite normalization values are from McDonough and Sun (1995).

inclusions. In contrast, Sm, Yb, and Lu show significant zoning with higher values in the cores of grains. Hafnium concentrations are just above detection limits and show broad decreases from core to rim (Fig. 8c).

DISCUSSION

Zircon growth, Pb-loss, and re-equilibration

Prior studies have documented that zircon U-Pb ages and zircon trace-element compositions can track crystallization, differentiation, and incremental emplacement of magmas (e.g., Coleman et al. 2004; Samperton et al. 2015). Many of these examples use zircon U-Pb data to show that intermediate to silica-rich plutons comprise numerous intrusive pulses. In the case of the Malaspina Pluton, our CA-ID-TIMS zircon ages are interpreted to reflect igneous crystallization over ca. 2.6 m.y. and this range in age may in part reflect pulses of intrusion. The stair-step array of younger SHRIMP-RG zircon ages from 116 to 110 Ma overlaps with the 113 Ma age of peak granulite metamorphism and partial melting from garnet ages (Fig. 10). We interpret these arrays of younger ages to reflect metamorphic zircon growth or recrystallization. Garnet and some of the zircon grain segments with younger ages may have grown simultane-

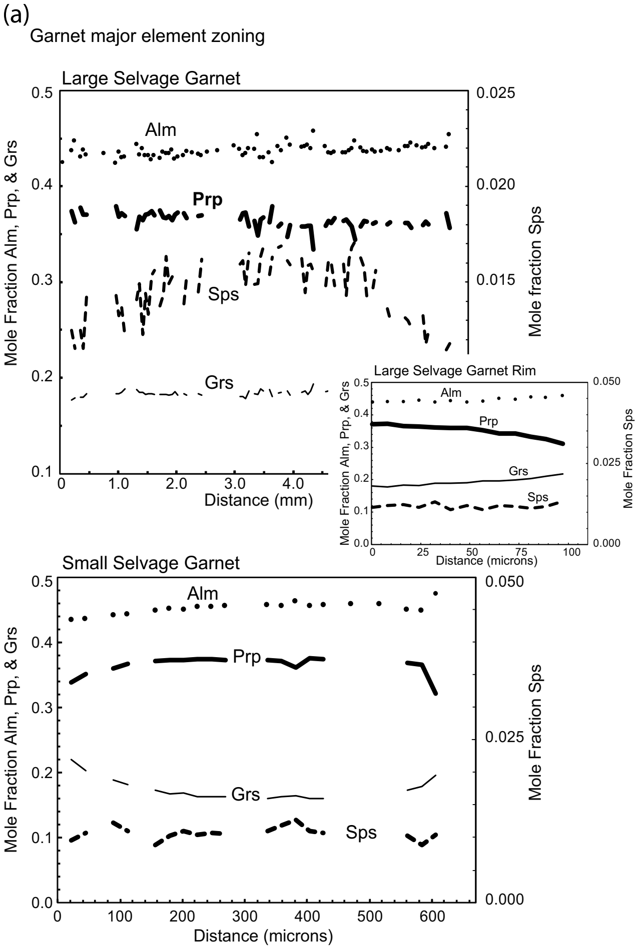

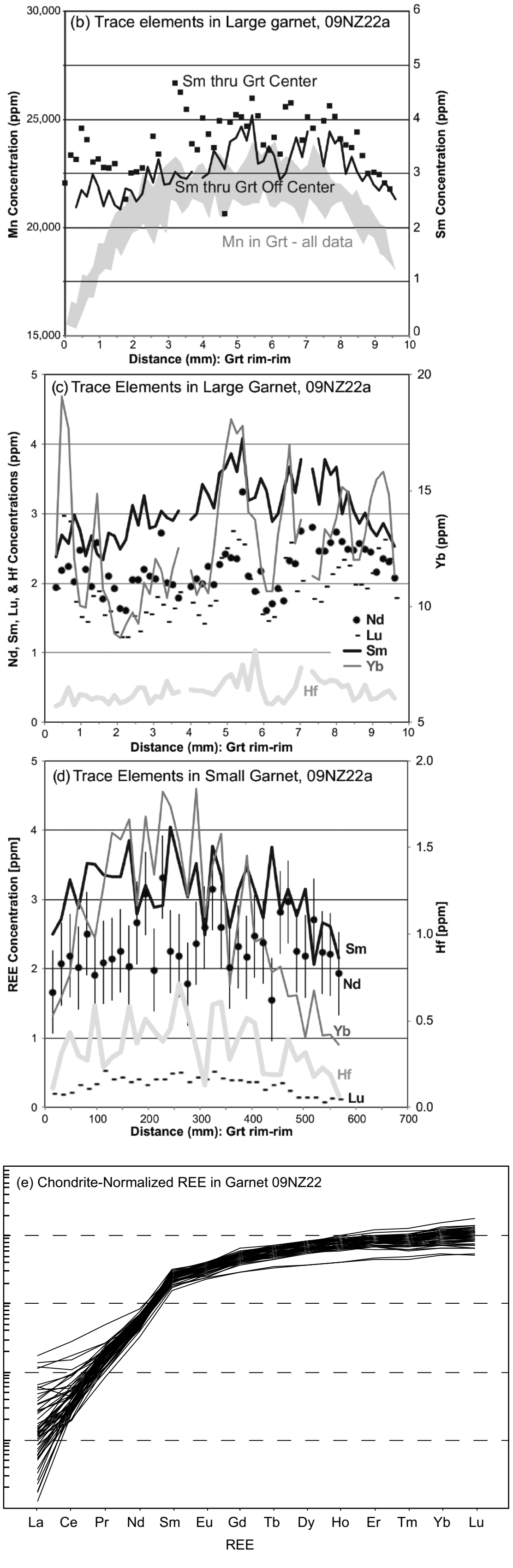

FIGURE 8. Garnet compositions in migmatite sample 09NZ22 from Crooked Arm New Zealand. (**a**) Mole fractions of almandine (Alm), pyrope (Prp), spessartine (Sps), and grossular (Grs) in large (~1 cm) garnet from vein selvages in sample 09NZ22a. Small garnet in the selvages lack high-Sps cores and show limited zoning that mimics the outermost rims of large grains. (**b**) Sm and Mn concentrations in large, ~10 mm diameter, selvage garnet. Data shown here were extracted from maps in Stowell et al. (2014) and were obtained by laser ablation ICP-MS. Data "Thru Grt Center" are the from the middle row of a rectangular grid through the geometric center of the grain. "Grt Off Center" are from row of analytical pits adjacent to center line. (**c**) Sm, Nd, Yb, Lu, and Hf concentrations for the same large selvage garnet shown in **a**. Nd and Hf are unzoned or weakly zoned. Yb, Lu, and Hf have oscillatory zoning. Zirconium (not shown for clarity) shows near identical oscillations to Yb. Data are a subset of those shown in maps from Stowell et al. (2014) and were obtained by LA-ICP-MS. (**d**) Sm, Nd, Yb, Lu, and Hf concentrations in small, ~0.6 mm, GRZ garnet. Note the lack of systematic zoning in Nd and Hf, and weak zoning in Sm and Lu with higher concentrations in the core, and similar, but more pronounced zoning in Yb. Two σ uncertainties are only shown for Nd for the sake of clarity. However, 2σ uncertainties in Hf, Lu, Sm, and Yb are ~±0.1 ppm. Data were obtained by high-resolution Element 2 LA-ICP-MS. (**e**) Chondrite-normalized REE values for garnet, 09NZ22. The steep slope from La to Gd and low slope from Gd to Lu at values from 20 to >100 is compatible with HREE sequestration into another mineral (see text for discussion). Chondrite normalization values are from McDonough and Sun (1995).

ously. Chondrite-normalized REE plots show moderate positive slopes for HREE in zircon and flat slopes in garnet similar to those observed in these minerals from other migmatites (e.g., Rubatto 2002). These patterns support the growth of garnet with zircon present or synchronous with late zircon that is supported by their overlapping isotopic ages.

The zircons from host orthogneiss and garnet granulite reaction zone have complex morphologies and CL responses, which illustrate distinct and contrasting textural characteristics (Fig. 3). In addition, the two U-Pb data sets presented here for treated (CA-TIMS) and untreated (SHRIMP-RG) zircon have significant ranges in dates and trace-element concentrations. We utilize zircon ages and trace-element compositions to construct a model for multiple batchwise igneous intrusions and subsequent metamorphism. The ages and trace elements allow us to estimate a minimum duration for intrusion, cooling rates for the Malaspina Pluton, and the time between intrusion and garnet granulite metamorphism.

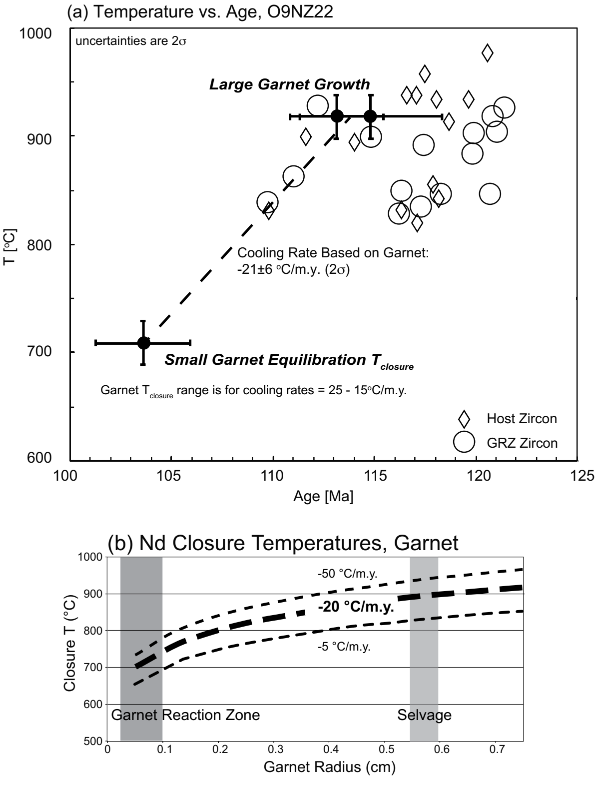

FIGURE 9. Temperature and age estimates for zircon and garnet from 09NZ22, Crooked Arm, New Zealand. (**a**) Temperature vs. age. Garnet data include Lu-Hf and Sm-Nd ages from ~12 mm grains and Sm-Nd ages for small grains (Table 3). The temperature estimates for garnet growth are based on *P-T* pseudosections in Stowell et al. (2014). A best-fit line from garnet growth to Sm and Nd closure in the small garnet grains indicates a cooling rate of ~20 °C/m.y. similar to the general trend of temperature vs. age estimates for zircon temperatures. (**b**) Closure temperature estimates for Nd diffusion in garnet. Ti-in-zircon temperatures (Table 2) were calculated with Si activities of 0.8 and Ti activities of 0.7. All Ti in zircon temperatures are corrected to $P = 1.4$ GPa using the dependence presented in Ferriss et al. (2008). Uncertainties for these Ti-in-zircon temperatures are likely to be >60 °C. Closure temperature estimates are based on the diffusion equations in Bloch et al. (2020), see Table 4.

We consider three end-member alternatives to explain the observed zircon ages, lithologic variations, and textural relationships (Fig. 11). All three of these scenarios could include multiple zircon growth episodes and minor Pb-loss during garnet granulite metamorphism.

In the first scenario, the garnet reaction zones and veins formed during metamorphism and partial melting of homogenous Malaspina Pluton host. The garnet reaction zone was near identical in igneous mineralogy to the host rock and subsequently recrystallized into garnet + clinopyroxene + partial melt with local melt migration into the adjacent trondhjemite veins. These veins, which are low in potassium and include very little potassium feldspar, are modified partial-melt compositions and evolved due to fractional crystallization and movement of melt out of the local melt production zones. Initial zircon growth occurred during crystallization of magma in the pluton between 118 and 116 Ma. This was followed by possible narrow zircon rim growth (e.g., GRZ-4.2 at 112.3 ± 2.4), local zircon resorption, and possible Pb-loss from zircon during metamorphism and partial melting from 115 to 111 Ma. In this scenario, melts and fluids would be most likely to promote metamorphic zircon growth and modification within the garnet reaction zone. Younger zircon growth and re-equilibration partial resorption of pre-existing zircon would be spatially restricted depending on fluid and melt

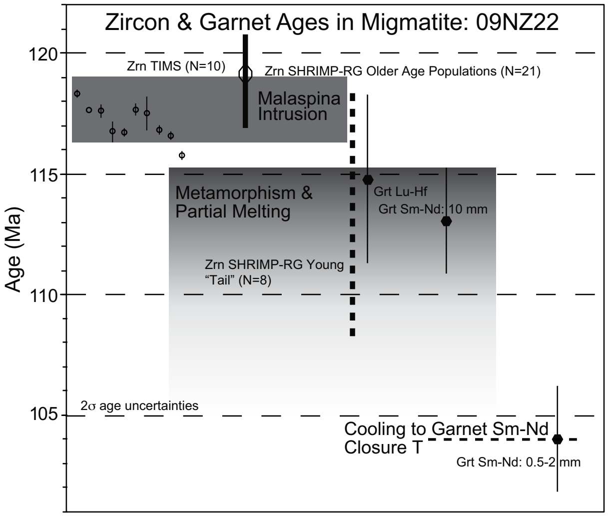

FIGURE 10. Comparison of all age results for zircon and garnet in migmatite from 09NZ22, Crooked Arm New Zealand. The ten individual CA-TIMS zircon results are shown as solid circles, the older SHRIMP-RG zircon results are shown as a solid line indicating the range of weighted mean ages for GRZ and Host age populations, the younger SHRIMP-RG zircon age range is show as a dashed line. The shaded area from 119 to 116.3 Ma shows the age range for 9 of the 10 zircon CA-TIMS ages, which overlap with the two older SHRIMP-RG age populations. This range is interpreted as the age of intrusion for the Malaspina Pluton in this part of Crooked Arm. The peak of metamorphism and garnet growth are taken as the overlap between Lu-Hf and Sm-Nd ages for large (~1 cm) grains. The thin dashed line at 104 Ma indicates the time for closure of small garnet grains to diffusion of Sm and Nd. The shaded gradient shows the interpreted age for garnet growth and the peak of garnet granulite metamorphism (115.4 to 111.3 Ma) down to closure of small garnet to Sm and Nd diffusion (ca. 104 Ma).

availability. Early magmatic zircon trace-element compositions would be relatively uniform due to the initial homogeneous rock in what is now the host and garnet reaction zone. The two distinct Th-U trends (Fig. 7d) reflect the separate evolution of the host Malaspina Pluton and the partial melt, which migrated toward and into the vein. Th/U vs. Hf zircon groups (Fig. 7e) reflect crystallization of the primary Malaspina Pluton magma and later partial melting.

In the second scenario, the garnet reaction zone formed from externally derived melt that was injected into fractures forming veins within a relatively homogeneous host pluton. Some of this melt then percolated into the adjacent host, and this was accompanied by recrystallization of the host to make the garnet + clinopyroxene + plagioclase-rich assemblage characteristic of the garnet reaction zone. As interpreted for the first scenario, zircon first grew during crystallization of the Malaspina Pluton between 118 and 116 Ma, followed by limited zircon growth (e.g., GRZ-4.2 at 112.3 ± 2.4 Ma) and modification during intrusion of the externally derived magma. Zircon in the garnet reaction zone would be a combination of relict grains (partly resorbed with possible Pb-loss) and new grains crystallizing from melt injection into the leucocratic veins and adjacent host forming the garnet reaction zone. Zircon trace-element compositions would be distinct with an initial pluton population and a secondary magma population related to magma in the vein. The two distinct Th/U trends (Fig. 7d) reflect the separate evolution of the host Malaspina Pluton and the younger melt injected into the vein. Th/U vs. Hf zircon groups (Fig. 7e) reflect crystallization of the primary Malaspina Pluton magma and later magma. Overlap between the compositional groups reflects physical mixing and overgrowths.

In the third scenario, the garnet reaction zones and veins formed during metamorphism of initially heterogeneous Malaspina Pluton. The garnet reaction zone had a distinct composition from the rock that was sampled as host. Although variations in the primary pluton mineralogy and composition are masked by LS deformation fabrics (Fig. 2b), igneous layering and/or dikes are common along Crooked Arm (Fig. 2a) and may have been present at the 09NZ22 sample location. Primary lithologic variation could be related to cryptic compositional layering, perhaps leading to significant variation in hydrous phases and solidus temperature. In this scenario, the garnet reaction zone formed from recrystallization and partial melting of a compositional domain in the pluton, which differed slightly from the host sample. Melting was more prevalent in the garnet reaction zone than in the host due to the initial bulk compositions. Similar to the first scenario, zircon grew during initial pluton crystallization between ca. 118 and 116 Ma and the two distinct Th-U trends (Fig. 7d) developed at this time. These trends reflect the different rock compositions in the host and garnet reaction zone. The igneous zircon was later locally modified and overgrown (e.g., GRZ-4.2 at 112.3 ± 2.4) during partial melting between 115 and 111 Ma. The youngest SHRIMP-RG ages reflect these processes, but the two distinct Th-U trends and Th/U vs. Hf zircon groups (Figs. 7d and 7e) reflect the separate evolution of two primary host Malaspina Pluton magmas.

In all of these three scenarios, the youngest melts in the garnet reaction zone would have reacted with minerals as melt fluxed through the solid matrix (e.g., Stuart et al. 2018). This reactive transport at temperatures in excess of 800 °C would likely lead to complete equilibration of some phases but not others. For example, zircon SHRIMP-RG age ranges and their trace-element concentrations and compositional trends (Fig. 7) are compatible with progressive changes occurring during growth in equilibrium with melts. The distinct clustering of zircon compositions with minor overlap between those in the host and garnet reaction zone best fit the third scenario. Therefore, we tentatively infer that the zircon data reflect two distinct igneous crystallization histories for the two samples from Crooked Arm and later partial modification during granulite facies metamorphism. However, the likelihood of significant compositional changes during reactive flux of melt through the garnet reaction zone remains a possible explanation for the observations.

The ages, compositions, and CL images for zircon presented here indicate the difficulty in using these observations for interpreting rock history. There are subtle differences in the

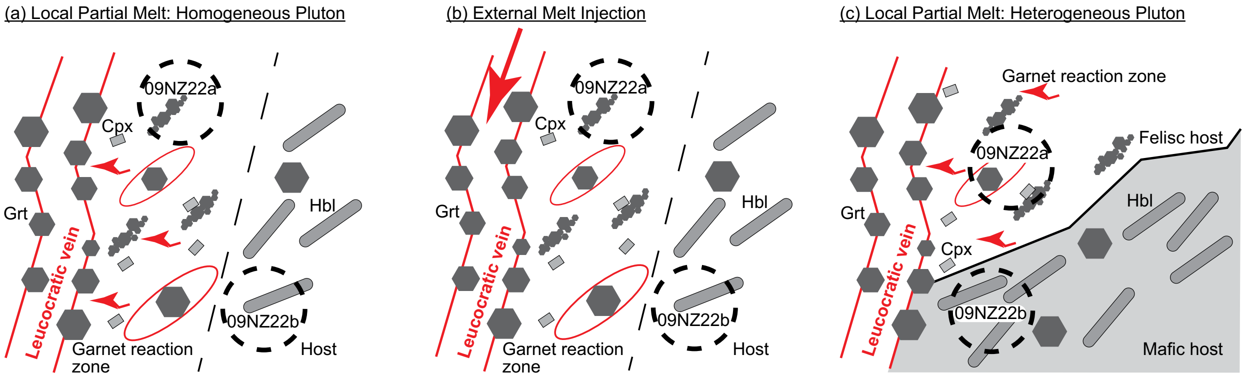

FIGURE 11. Illustrations showing the 3 scenarios proposed for melt sources during garnet granulite metamorphism. (**a**) Partial melting of homogeneous Malaspina Pluton. (**b**) Injection of externally sourced leucocratic melt into a vein. (**c**) Partial melting of a felsic layer within the heterogeneous Malaspina Pluton. All of these three scenarios produce leucocratic veins, garnet selvages, and garnet reaction zones. The leucocratic veins are ~5 cm wide. See text for details. Red lines enclose areas of partial melt and the black dashed circles indicate two of the samples discussed in the text as host (09NZ22b) and garnet reaction zone (09NZ22a). Cpx = clinopyroxene, Grt = garnet, Hbl = hornblende. (Color online.)

morphology and CL images between zircon in the garnet reaction zone vs. the host. Garnet reaction zone zircons are anhedral with numerous embayments, and the CL images indicate a lack of coherent oscillatory zoning. In contrast, the host zircons are mostly rounded in form and have both sector and oscillatory CL zoning. However, these differences do not correlate clearly with age. Much of the soccer ball zircon with diffuse oscillatory zoning in the Malaspina Pluton has been interpreted as igneous (e.g., Stowell et al. 2014; Schwartz et al. 2017) and our data generally support this interpretation. The largely soccer ball zircons in the host have SHRIMP-RG ages that range from the oldest to the youngest values observed in the Malaspina Pluton along Crooked Arm. Our data indicate that these oscillatory zoned zircons may not have been closed to U and Pb because individual spot ages from areas with the same type of CL response have ages that vary by more than 5 m.y.

Trace-element concentrations and ratios in coexisting minerals are a powerful tool for evaluating equilibrium (e.g., Rubatto 2002). In some cases, trace-element data for a single mineral provide important information about equilibrium of a mineral with phases not currently found in the sample (e.g., Wood et al. 2013; Rubatto et al. 2007). In addition, trivalent and quadrivalent ion ratios in zircon provide constraints on igneous fractionation and possible diffusion. Th/U ratios have been considered a tool for discriminating between igneous and metamorphic zircon (e.g., Rubatto 2002). Many metamorphic zircons have Th/U ratios <0.1 due to the very low availability of Th and or partitioning into other phases during metamorphism. This is at best imperfect because, as summarized by Harley et al. (2007), there are abundant examples of zircon that cannot be correctly classified with this discrimination ratio. However, Th/U ratios may reflect crystallization and evolution of a magma. In the migmatite from Crooked Arm, distinct trends in Th vs. U and Th/U vs. age (Fig. 7) are compatible with differing and distinct primary magmas in these rocks. In the garnet reaction zone, partial melting and possible melt injection resulted in a more silica-rich composition than bulk Malaspina magmas, and we infer that these processes failed to erase the distinct zircon signatures.

Assuming that all of the CA-TIMS zircon ages reflect igneous crystallization, then they indicate the minimum duration of Malaspina intrusion and crystallization. These zircon age ranges are from 118.4 to 116.6 Ma with a duration of 1.8 m.y., and 117.9 to 115.5 Ma with a duration of 2.4 m.y. for the host and garnet reaction zone, respectively. Because the age ranges only overlap in part, the age range for both data sets is from 118.4 to 115.5 Ma and the duration is 2.9 m.y. for the Malaspina Pluton along this part of Crooked Arm.

Garnet ages as a reflection of peak and post-peak metamorphism

Large garnets have low-amplitude major element zoning with bell-shaped gradients in mole fraction of spessartine (Sps) and pronounced variations in trace element concentrations (Fig. 8). The sharp concentration gradients in REE are defined by multiple analyses for each concentric band (Fig. 8) and are interpreted as growth zoning (Stowell et al. 2014). Sm, Nd, and Lu concentrations vary by ~1.5 ppm, and Yb by >3 ppm. These major and trace element variations suggest that diffusion of major elements may have been significant but that there was little or no significant diffusion of REE within the large garnet grains. Closure temperatures in garnet are useful for evaluating cooling histories (e.g., Dodson 1973; Ganguly et al. 1998; Ganguly and Tirone 1999), and we adopt the simple closure temperature formulation of Dodson (1973) because the garnet reaction zone grains are interpreted to have been completely modified by diffusion, the surrounding melt can be approximated as a homogenous matrix, and finally for slow cooling and small grain sizes the closure temperature models converge (Ganguly et al. 1998; Ganguly and Tirone 1999). Closure temperatures for Nd diffusion were estimated using the slow diffusion formulation of Bloch et al. (2020), appropriate for high pressure, and compared to that of Carlson (2012). The results (Table 4) indicate that the largest grains with 5–6 mm radius would have closure temperatures of 870 to 1090 °C with cooling rates of 15 to 25 °C/m.y. Therefore, regardless of formulation, the Sm-Nd ages for large garnet should approximate the timing of peak metamorphism. The Lu-Hf age of 115 Ma is tentatively preferred over ages calculated with surrounding minerals because Lu-Hf ages should be biased toward core growth (e.g., Lapen 2003) and significant diffusion of Lu and Hf would require higher temperatures than Sm and Nd (e.g., Carlson 2012; Bloch et al. 2020), resulting in older Lu-Hf ages. Trace element zoning in garnets is compatible with little or diffusion of REE and Hf in large garnet (Fig. 8), and the two isotopic systems result in indistinguishable ages. However, the 4 m.y. uncertainty for the garnet Lu-Hf age of 115 Ma is too large for a definitive interpretation of any age difference between the two isotopic systems.

Small garnet grains have little zoning in major elements, lack high-spessartine cores, and show pyrope and increased grossular close to the rims (Fig. 8a). These small-scale trends in major element concentrations mimic those found in the outermost rims of the large grains. The trace element concentrations in small garnet show zigzag patterns anchored by single analyses (Fig. 8d). The cause of this variation, which exceeds analytical uncertainty, is unknown; however, it may result from inclusions. Ignoring these oscillations, Sm and Nd show little or no variation, and Yb, Hf, and Lu show low-amplitude variation with high-core and lower-rim concentrations. Based on the compositional zoning, the 103.6 Ma garnet Sm-Nd age for small garnet reaction zone grains could reflect late garnet growth or isotopic re-equilibration during cooling. We infer that these small grains exchanged REE with clinopyroxene and or apatite, both of which are intergrown with garnet in the garnet reaction zone. The Nd closure temperatures for garnet based on Bloch et al. (2020) are 690, 700, and 710 °C for 0.5 mm radius and cooling rates of –15, –20, and –25 °C/m.y., respectively (Table 4). The garnet textures (Fig. 2) are most compatible with synchronous growth of Type 1 and 2 garnet during vein emplacement; therefore, we infer that Type 2 garnet was significantly modified by diffusion and use the closure temperature to calculate cooling rates below.

Cooling rates determined from zircon and garnet

The most comprehensive high-precision, SHRIMP-RG zircon age results for the Malaspina Pluton (Schwartz et al. 2017; and herein) indicate that most of the magma intruded ca. 118–116 Ma. Initial cooling occurred in the lower crust prior to significant extension at ca. 108–106 Ma (Stowell et al. 2014; Schwartz et al. 2016; Klepeis et al. 2016). Garnet Sm-Nd ages from across the Misty and Malaspina plutons indicate that garnet granulite metamorphism of the plutons was at 111.7 ± 1.0 Ma, ca. 5 m.y. after intrusion (Stowell et al. 2014, 2017). Either the pluton cooled slowly and remained hot through garnet growth, or initial cooling was followed by reheating to ~920 °C triggering local garnet growth. In the first scenario, a local trigger for partial melting and garnet growth is required. This could have been volatile flux with or without externally derived melt (Clarke et al. 2005). However, abundant Type 3 isolated garnet grains with leucosome halos, variably distributed in the Malaspina Pluton, indicate that local garnet growth was independent of external fluids and magma veins. Therefore, we infer that much or all garnet growth resulted from post-emplacement heating of the heterogeneous pluton.

Metamorphic temperature estimates, the age of large garnet, and the Nd closure temperatures for small garnet (Table 4) provide a means for calculating the cooling rate. Choosing a radius of 0.5 mm for small garnet, iterative calculation of the cooling rate and the garnet closure temperature results in best estimates of ~20 °C/m.y. and ~700 °C (Fig. 9). This cooling rate is similar to the approximate slope for the array of Ti in zircon temperatures and corresponding U-Pb ages (Fig. 9). The cooling rate estimated here is approximately half the ~50 °C/m.y. estimated from zircon and titanite ages in Flowers et al. (2005) and higher than estimates of 8–14 °C m.y. in Schwartz et al. (2016).

IMPLICATIONS

The identification of igneous and metamorphic zircon grains, overgrowths of metamorphic zircon on prior crystals, and zircon affected by Pb loss cannot always be made from CL images and crystal morphology in migmatitic granulite facies rocks. This observation is supported by several data sets: (1) the large range of ages for each zircon morphology and CL type; (2) the near-complete lack of clearly igneous prismatic grain shapes in both host and garnet reaction zone lithologies; (3) the significant population of zircon U-Pb ages that match ages for igneous crystallization determined for Malaspina Pluton samples with primary igneous textures; and (4) the 11–14 m.y. range (considering uncertainties) of concordant SHRIMP-RG U-Pb ages determined from targeted CL spots. Finally, the overlap of younger zircon U-Pb ages with Sm-Nd and Lu-Hf ages for metamorphic garnet growth cannot be readily correlated with internal CL textures in zircon grains or to possible Pb loss from zircon.

Assigning SHRIMP-RG U-Pb zircon ages to intrusion vs. later metamorphism and partial melting is difficult in our data set due to the large range in dates from >118 to <110 Ma. In addition, the two core rim pairs include one with normal and one with reverse age zoning. Therefore, we conclude that multiple isotope data sets from several samples are essential for unraveling the igneous and metamorphic history of migmatites.

Unraveling the history of this lower crustal migmatite is complicated by inferred premetamorphic igneous complexity. The range in CA-TIMS zircon ages and distinct groups in Sm, Yb, Ce, and Eu values vs. Hf (Figs. 7a and 7b) are compatible with more than one magma. This is supported by field evidence for incremental construction of the Malaspina Pluton by sheeted intrusion into a crystal mush zone (Klepeis et al. 2016). The zircon dates and compositions are compatible with two distinct magmas that crystallized between 118 and 116 Ma that underwent different fractional crystallization trends evident in the "host" and garnet reaction zone samples. Deformation, which produced the LS fabric has obscured textural evidence for the contact between these intrusions and some magma mixing is possible. In addition, the garnet reaction zone leucosome may include melt injected into the partially melted garnet reaction zone from the vein.

Intracrystalline diffusion of trace elements was insignificant in large garnet grains. The oscillatory and bell-shaped trace element zoning in garnet indicates that diffusion has played a limited role in garnet trace element distributions. In addition, calculated closure temperatures indicate that modification of REE by diffusion could not have affected the interiors of these crystals. We conclude that large euhedral garnet can preserve growth ages recorded by both Lu-Hf and Sm-Nd systems with uncertainties of ca. 2 m.y.

Zircon and garnet ages indicate a brief interval between pluton emplacement and garnet growth (Fig. 10). The CA-TIMS U-Pb zircon ages of 118.3–115.7 and garnet ages of ca. 113 Ma require 2.7 to 5.3 m.y. between pluton crystallization and granulite metamorphism. This temperature increase shortly after intrusion is compatible with a magmatic pulse. No magmas of this age are known in the Western Fiordland Orthogneiss and the granulite event is tentatively attributed to magmatic underplating.

Zircon SHRIMP-RG ages of ca. 121 and 115 Ma anchor the high-temperature ends of two Ti in zircon temperature–age clusters, which could represent distinct crystallization trends. Garnet Sm-Nd growth and cooling ages overlap with the younger of these clusters indicating a cooling rate of ~20 °C/m.y. from 920 to about 700 °C after the peak of granulite metamorphism. Cooling rates for the lower crust of a continental magmatic arc are difficult to obtain due to limited exposure and geological complexity. Mid- to lower-crustal rocks of the Coast Mountains batholith in Canada cooled 2 to 11 °C/m.y. after granulite facies metamorphism at pressures of ~10 kbar (Hollister 1982; Rusmore et al. 2005). The data for lower crustal rocks in the Coast Mountains and Fiordland are taken to indicate that the lower crust of continental magmatic arcs may cool at rates <25 °C/m.y.

The mid- to lower-crustal emplacement of the Malaspina Pluton and lack of supracrustal rocks with a metamorphic history shared with these rocks preclude the construction of a significant prograde path. However, the ~20 °C/m.y. cooling rate for a single location in the Malaspina Pluton provides a robust estimate for cooling from ~920 to 700 °C. Additional data are needed to evaluate the spatial extent and variation of cooling rates across the lower crustal rocks in Fiordland. This new cooling rate for the Crooked Arm outcrop is far slower than estimates for cooling of granulite in the U.S.A. Adirondacks (Storm and Spear 2005) or initial cooling of Dora Maira Massif in the Western Alps (Engi et al. 2017), but similar to estimates for cooling of ultrahigh-temperature granulite from the Saxon Granulite Massif in Germany (Romer and Rötzler 2001). Both of these examples are constructed from composite *P-T-t* paths and/or diffusion models, which include data input from multiple samples. Large data sets of comprehensive linked *P-T-t* data for individual outcrops are needed to better understand tectonic histories in lower crustal rocks in Fiordland and elsewhere.

ACKNOWLEDGMENTS AND FUNDING

The authors thank Jeff Vervoort at Washington State University and Kenneth Horkley for assistance with garnet Lu-Hf geochronology, Karen Odom Parker at the University of Alabama for assistance in establishing the UA RadIs lab, Alan Koenig (U.S. Geological Survey) and Zahn Peng (California State University at Northridge) for help obtaining trace-element garnet data, and Matthew Coble for assistance with the SHRIMP-RG data. This work could not have been completed without National Science Foundation grant EAR 1119039, which supported establishment of the UA RadIs laboratory. SHRIMP-RG zircon dating was supported by NSF EAR-1352021.

REFERENCES CITED

Allibone, A.H., Jongens, R., Scott, J.M., Tulloch, A.J., Turnbull, I.M., Cooper, A.F., Powell, N.G., Ladley, E.B., King, R.P., and Rattenbury, M.S. (2009) Plutonic rocks of the Median Batholith in eastern and central Fiordland, New Zealand: Field relations, geochemistry, correlation, and nomenclature. New Zealand Journal of Geology and Geophysics, 52, 101–148.

Baxter, E.F., and Scherer, E.E. (2013) Garnet: Timekeeper of tectonometamorphic processes. Elements, 9, 433–438.

Baxter, E.F., Caddick, M.J., and Dragovic, B. (2017) Garnet: a rock forming mineral petrochronometer. Reviews in Mineralogy and Geochemistry, 83, 469–533.

Begemann, F., Ludwig, K.R., Lugmair, G.W., Min, K., Nyquist, L.E., Patchett, P.J., Renne, P.R., Shih, C.-Y., Villa, I.M., and Walker, R.J. (2001) Call for an improved set of decay constants for geochronological use. Geochimica et Cosmochimica Acta, 65, 111–121.

Blattner, P. (1976) Replacement of hornblende by garnet in granulite facies assemblages near Milford Sound, New Zealand. Contributions to Mineralogy and Petrology, 55, 181 –190.

Bloch, E.M., Jollands, M.C., Devoir, A., Bouvier, A.-S., Ibañez-Mejia, M., and Baumgartner, L.P. (2020) Multispecies diffusion of yttrium, rare earth elements and hafnium in garnet. Journal of Petrology, 61(7), egaa055.

Bowring, J.F., McLean, N.M., and Bowring, S.A. (2011) Engineering cyber infrastructure for U-Pb geochronology: Tripoli and U-Pb_Redux. Geochemistry, Geophysics, Geosystems, 12, 1–19.

Bradshaw, J.Y. (1989) Origin and metamorphic history of an Early Cretaceous polybaric granulite terrain, Fiordland, southwest New Zealand. Contributions to Mineralogy and Petrology, 103, 346–360.

Carlson, W. (2012) Rates and mechanism of Y, REE, and Cr diffusion in garnet. American Mineralogist, 97, 1598–1618.

Carty, K., Schwartz, J., Wiesenfeld, J., Klepeis, K., Stowell, H.H., Tulloch, A., and Barnes, C.G. (2021) Magma chamber geometry and melt interconnectivity in the lower crust of a continental arc, Fiordland, New Zealand. Journal of Petrology, 62, 9, 1-41.

Cheng, H., King, R.L., Nakamura, E., Vervoort, J.D., and Zhou, Z. (2008) Coupled Lu-Hf and Sm-Nd geochronology constrains garnet growth in ultra-high-pressure eclogites from the Dabie orogen. Journal of Metamorphic Geology, 26, 741–758.

Clarke, G.L., Daczko, N., Klepeis, K.A., and Rushmer, T. (2005) Roles for fluid and/or melt advection in forming high-P mafic migmatites, Fiordland, New Zealand. Journal of Metamorphic Geology, 23, 557–567.

Coble, M.A., Vazquez, J.A., Barth, A.P., Wooden, J., Burns, D., Kylander-Clark, A., Jackson, S., and Vennari, C.E. (2018) Trace element characterization of MAD-559 zircon reference material for ion microprobe analysis. Geostandards and Geoanalytical Research, 42, 481–497.

Coleman, D.S., Gray, W., and Glazner, A.F. (2004) Rethinking the emplacement and evolution of zoned plutons: Geochronologic evidence for incremental assembly of the Tuolumne Intrusive Suite, California. Geology, 32, 433–436.

Condon, D.J., Schoene, B., McLean, N.M., Bowring, S.A., and Parrish, R.R. (2015) Metrology and traceability of U–Pb isotope dilution geochronology (EARTHTIME Tracer Calibration Part I). Geochimica et Cosmochimica Acta, 164, 464–480.

Daczko, N.R., and Halpin, J.A. (2009) Evidence for melt migration enhancing recrystallization of metastable assemblages in mafic lower crust, Fiordland, New Zealand. Journal of Metamorphic Geology, 27, 167–185.

Daczko, N., Piazolo, S., Meek, U., Stuart, C.A., and Elliott, V. (2016) Hornblendite delineates zones of mass transfer through the lower crust. Scientific Reports, 6, 31369.

Decker, M., Schwartz, J.J., Stowell, H.H., Klepeis, K.A., Tulloch, A.J., Kitajima, K., Valley, J.W., and Kylander-Clark, A.R.C. (2017) Slab-triggered arc flare-up in the Cretaceous median batholith and the growth of lower arc crust, Fiordland, New Zealand. Journal of Petrology, 58, 1145–1172.

Dodson, M.H. (1973) Closure temperatures in cooling geochronological and petrological systems. Contributions to Mineralogy and Petrology, 40, 259–274.

Donovan, J. (2010) Probe for EPMA, Eugene, Oregon, Probe Software. https://www.probesoftware.com/index.html (accessed June 2019).

Ducea, M.N., Saleeby, J.B., and Bergantz, G. (2015) The architecture, chemistry, and evolution of continental magmatic arcs. Annual Review of Earth and Planetary Sciences, 43, 299–331.

Engi, M., Lanari, P., and Kohn, M.J. (2017) Significant ages—An introduction to petrochronology. In M.J. Kohn, M. Engi, and P. Lanari, Eds., Petrochronology: Methods and Applications, 83, 1–12. Reviews in Mineralogy and Geochemistry, Mineralogical Society of America, Chantilly, Virginia.

Ferriss, E.D.A., Essene, E.J., and Becker, U. (2008) Computational study of the effect of pressure on the Ti-in-zircon geothermometer. European Journal of Mineralogy, 20, 745 –755.

Ferry, J.M., and Watson, E.B. (2007) New thermodynamic models and revised calibrations for the Ti-in-zircon and Zr-in-rutile thermometers. Contributions to Mineralogy and Petrology, 154, 429–437.

Flowers, R.M., Bowring, S.A., Tulloch, A.J., and Klepeis, K.A. (2005) Tempo of burial and exhumation within the deep roots of a magmatic arc, Fiordland, New Zealand. Geology, 33, 17–20.

Ganguly, J., and Tirone, M. (1999) Closure temperature, cooling age and high temperature thermochronology. In A.K. Gupta and S. Dasgupta, Eds., Physics and chemistry of the Earth's interior: Crust, mantle and core, 89–98. Indian National Science Academy-Springer (India).

Ganguly, J., Tirone, M., and Hervig, R. (1998) Diffusion kinetics of samarium and neodymium in garnet and a method for determining cooling rates of rocks. Science, 281, 805–807.

Gatewood, M.P., Dragovic, B., Stowell, H.H., Baxter, E.F., Hirsch, D.M., and Bloom, R.A. (2015) Evaluating chemical equilibrium in metamorphic rocks using major element and Sm-Nd isotopic age zoning in garnet, Townsend Dam, Vermont, U.S.A. Chemical Geology, 401, 151–168.

Gibson, G.M., and Ireland, T.R. (1995) Granulite formation during continental extension in Fiordland. Nature, 375, 479–482.

Gibson, G.M., McDougall, I., and Ireland, T.R. (1988) Age constraints on metamorphism and development of a metamorphic core complex in Fiordland, southern New Zealand. Geology, 16, 405–408.

Hacker, B.R., Mehl, L., Kelemen, P.B., Rioux, M., Behn, M.D., and Luffi, P. (2008) Reconstruction of the Talkeetna intraoceanic arc of Alaska through thermobarometry. Journal of Geophysical Research, 113, BO3204.

Hammerli, J., Kemp, A.I.S., Shimura, T., Vervoort, J.D., EIMF, and Dunkley, D.J. (2018) Generation of I-type granitic rocks by melting of heterogeneous lower crust. Geology, 46, 907–910.

Harley, S.L., Kelly, N.M., and Möller, A. (2007) Zircon behavior and the thermal histories of mountain chains. Elements, 3, 25–30.

Hollis, J.A., Clarke, G.L., Klepeis, K.A., Daczko, N.R., and Ireland, T.R. (2004) The regional significance of Cretaceous magmatism and metamorphism in Fiordland, New Zealand, from U-Pb zircon geochronology. Journal of Metamorphic Geology, 22, 607–627.

Hollister, L.S. (1982) Metamorphic evidence for rapid (2 mm/yr) uplift of a portion of the Central Gneiss Complex, Coast Mountains, B.C. Canadian Mineralogist, 20, 319 –332.

Hoskin, P.W.O., and Schaltegger, U. (2003) The composition of zircon and igneous and metamorphic petrogenesis. Reviews in Mineralogy and Geochemistry, 53, 27–62.

Jaffey, A.H., Flynn, K.F., Glendenin, L.E., Bentley, W.C., and Essling, A.M. (1971) Precision measurement of half-lives and specific activities of ^{235}U and ^{238}U. Physical Review C, 4, 1889–1906.

Jagoutz, O. (2010) Construction of the granitoid crust of an island arc. Part II: A quantitative petrogenetic model. Contributions to Mineralogy and Petrology, 160, 359–381.

Kay, R.W., and Mahlburg Kay, S. (1993) Delamination and delamination magmatism. Tectonophysics, 219, 177–189.

Klepeis, K.A., Clarke, G.L., and Rushmer, T. (2003) Magma transport and coupling between deformation and magmatism in the continental lithosphere. GSA Today, 13, 4–11.

Klepeis, K.A., Schwartz, J., Stowell, H., and Tulloch, A. (2016) Gneiss domes, vertical and horizontal mass transfer, and the initiation of extension in the hot lower crustal root of a continental arc, Fiordland, New Zealand. Lithosphere, 8, 116–140.

Krogh, T.E. (1973) A low-contamination method for hydrothermal decomposition of zircon and extraction of U and Pb for isotopic age determinations. Geochimica et Cosmochimica Acta, 37, 485–494.

Lapen, T.J., Johnson, C.M., Baumgartner, L.P., Mahlen, N.J., Beard, B.L., and Amato, J.M. (2003) Burial rates during prograde metamorphism of an ultra-high-pressure terrane: An example from Lago di Cignana, western Alps, Italy. Earth and Planetary Science Letters, 215, 57–72.

Lee, C.-T.A., Cheng, X., and Horodyskyj, U. (2006) The development and refinement of continental arcs by primary basaltic magmatism, garnet pyroxenite accumulation, basaltic recharge and delamination: insights from the Sierra Nevada, California. Contributions to Mineralogy and Petrology, 151, 222–242.

Ludwig, K.R. (2009) Squid 2: A User's Manual. Berkeley Geochronology Center Special Publication, 5, 1–110.

——— (2012) User's manual for Isoplot 3.75–4.15: A geochronological toolkit for Microsoft Excel. Berkeley Geochronology Center Special Publication, 5, 74.

Lugmair, G.W., and Marti, K. (1978) Lunar initial ^{143}Nd/^{144}Nd: differential evolution of the lunar crust and mantle. Earth and Planetary Science Letters, 39, 349–357.

Mattinson, J.M. (2005) Zircon U-Pb chemical abrasion ("CA-TIMS") method: Combined annealing and multi-step partial dissolution analysis for improved precision and accuracy of zircon ages. Chemical Geology, 220, 47–66.

Mattinson, J.M., Kimbrough, D.L., and Bradshaw, J.Y. (1986) Western Fiordland orthogneiss: Early Cretaceous arc magmatism and granulite facies metamorphism, New Zealand. Contributions to Mineralogy and Petrology, 92, 383–392.

McDonough, W.F., and Sun, S.S. (1995) The composition of the Earth. Chemical Geology, 120, 223–253.

McLean, N.M., Bowring, J.F., and Bowring, S.A. (2011) An algorithm for U-Pb isotope dilution data reduction and uncertainty propagation. Geochemistry, Geophysics, Geosystems, 1–26.

McLean, N.M., Condon, D.J., Schoene, B., and Bowring, S.A. (2015) Evaluating uncertainties in the calibration of isotopic reference materials and multi-element isotopic tracers (EARTHTIME Tracer Calibration Part II). Geochimica et Cosmochimica Acta, 164, 481–501.

Mezger, K., Essene, E.J., and Halliday, A.N. (1992) Closure temperatures of the Sm-Nd system in metamorphic garnets. Earth and Planetary Science Letters, 113, 397–409.

Milan, L.A., Daczko, N.R., Clarke, G.L., and Allibone, A.H. (2016) Complexity of in-situ zircon U-Pb-Hf isotope systematics during arc magma genesis at the roots of a Cretaceous arc, Fiordland, New Zealand. Lithos, 264, 296–314.

Oliver, G.J.H. (1977) Feldspathic hornblende and garnet granulites and associated anorthosite pegmatites from Doubtful Sound, Fiordland, New Zealand. Contributions to Mineralogy and Petrology, 65, 111–121.

——— (1980) Geology of the granulite and amphibolite facies gneisses of Doubtful Sound, Fiordland. New Zealand. New Zealand Journal of Geology and Geophysics, 23, 27–41.

Oliver, G.J.H., and Coggon, J.H. (1979) Crustal structure of Fiordland, New Zealand. Tectonophysics, 54, 253–292.

Paton, C., Hellstrom, J., Paul, B., Woodhead, J., and Hergt, J. (2011) Iolite: Freeware for the visualisation and processing of mass spectrometric data. Journal of Analytical Atomic Spectrometry, 26, 2508.

Ramezani, J., Hoke, G.D., Fastovsky, D.E., Bowring, S.A., Therrien, F., Dworkin, S.I., Atchley, S.C., and Nordt, L.C. (2011) High-precision U-Pb zircon geochronology of the Late Triassic Chinle Formation, Petrified Forest National Park (Arizona, USA): Temporal constraints on the early evolution of dinosaurs. Geological Society of America Bulletin, 123, 2142–2159.

Romer, R.L., and Rötzler, J. (2001) P-T-t Evolution of ultrahigh-temperature granulites from the Saxon Granulite Massif, Germany. Part II. Journal of Petrology, 42, 2015–2032.

Rubatto, D. (2002) Zircon trace element geochemistry: partitioning with garnet and link between U-Pb ages and metamorphism. Chemical Geology, 184, 123–138.

Rubatto, D., and Hermann, J. (2007) Zircon behaviour in deeply subducted rocks. Elements, 3, 31–35.

Rusmore, M.E., Woodsworth, G.J., and Gehrels, G.E. (2005) Two-stage exhumation of midcrustal rocks, Coast Mountains, British Columbia. Tectonics, 24, 1–25.

Samperton, K.M., Schoene, B., Cottle, J.M., Keller, C.B., Crowley, J.L., and Schmitz, M.D. (2015) Magma emplacement, differentiation and cooling in the middle crust: Integrated zircon geochronological–geochemical constraints from the Bergell Intrusion, Central Alps. Chemical Geology, 417, 322–340.

Scherer, E., Münker, C., and Mezger, K. (2001) Calibration of the lutetium-hafnium clock. Science, 293, 683–687.

Schwartz, J.J., Stowell, H.H., Klepeis, K., Zamora, C., Tulloch, A., Kylander-Clark, A., Hacker, B., and Coble, M. (2016) Thermochronology of extensional orogenic collapse in the deep crust, Fiordland, New Zealand. Geosphere, 12, 647–631.

Schwartz, J.J., Klepeis, K., Sadorski, J.F., Stowell, H.H., Tulloch, A., and Coble, M. (2017) The tempo of continental arc construction in the Mesozoic Median Batholith, Fiordland, New Zealand. Lithosphere, 9, 343–365.

Smit, M., Scherer, E., and Mezger, K. (2013) Lu-Hf and Sm-Nd garnet geochronology: Chronometric closure and implications for dating petrological processes. Earth and Planetary Science Letters, 381, 222–233.

——— (2014) Corrigendum to "Lu–Hf and Sm–Nd garnet geochronology: chronometric closure and implications for dating petrological processes" [Earth and Planetary Science Letters, 381 (2013), 222–233]. Earth and Planetary Science Letters, 391, 255.

Söderlund, U., Patchett, P.J., Vervoort, J.D., and Isachsen, C.E. (2004) The ^{176}Lu decay constant determined by Lu-Hf and U-Pb isotope systematics of Precambrian mafic intrusions. Earth and Planetary Science Letters, 219, 311–324.

Stacey, J.S., and Kramers, J.D. (1975) Approximation of terrestrial lead isotope evolution by a two-stage model. Earth and Planetary Science Letters, 26, 207–221.

Stevenson, J.A., Daczko, N.R., Clarke, G.L., Pearson, N., and Klepeis, K.A. (2005) Direct observation of adakite melts generated in the lower continental crust, Fiordland, New Zealand. Terra Nova, 17, 73–79.

Storm, L.C., and Spear, F.S. (2005) Pressure, temperature and cooling rates of granulite facies migmatitic pelites from the southern Adirondack Highlands, New York. Journal of Metamorphic Geology, 23, 107–130.

Stowell, H.H., Taylor, D.L., Tinkham, D.K., Goldberg, S.A., and Ouderkirk, K.A. (2001) Contact metamorphic *P-T-t* paths from Sm-Nd garnet ages, phase equilibria modeling, and thermobarometry: Garnet Ledge, Southeastern Alaska. Journal of Metamorphic Geology, 19, 645–660.

Stowell, H.H., Bulman, G.R., Zuluaga, C.A., Tinkham, D.K., And Miller, R.B. (2007) mid-crustal late cretaceous metamorphism in the Nason Terrane, Cascades Crystalline Core, Washington, U.S.A., implications for tectonic models. In R.D. Hatcher, Jr., M.P. Carlson, J.H. McBride, and J.R. Martínez Catalán, Eds., 4-D Framework of Continental Crust, 200, 211–231. Geological Society of America Memoir.

Stowell, H.H., Tulloch, A., Zuluaga, C.A., and Koenig, A. (2010) Timing and duration of garnet granulite metamorphism in magmatic arc crust, Fiordland, New Zealand. Chemical Geology, 273, 91–110.

Stowell, H.H., Odom Parker, K., Gatewood, M.P., Tulloch, A., and Koenig, A. (2014) Temporal links between pluton emplacement, garnet granulite metamorphism, partial melting, and extensional collapse in the lower crust of a Cretaceous magmatic arc, Fiordland New Zealand. Journal of Metamorphic Geology, 32, 151–175.

Stowell, H.H., Schwartz, J.J., Klepeis, K., Hout, C., Tulloch, A., and Koenig, A. (2017) Sm-Nd garnet ages for granulite and eclogite in the Breaksea Orthogneiss and widespread granulite facies metamorphism of the lower crust, Fiordland magmatic arc, New Zealand. Lithosphere, 9, 953–975.

Stuart, C.A., Meek, U., Daczko, N.R., Piazolo, S., and Huang, J.-X. (2018) Chemical signatures of melt-rock interaction in the root of a magmatic arc. Journal of Petrology, 59, 321–340.

Tanaka, T., Togashi, S., Kamioka, H., Amakawa, H., Kagami, H., Hamamoto, T., Yuhara, M., Orihashi, Y., Yoneda, S., Shimizu, H., and others (2000) JNdi-1: A neodymium isotopic reference in consistency with LaJolla neodymium. Chemical Geology, 168, 279–281.

Trail, D., Watson, E.B., and Tailby, N.D. (2012) Ce and Eu anomalies in zircon as proxies for the oxidation state of magmas. Geochimica et Cosmochimica Acta, 97, 70–87.

Tulloch, A.J., and Kimbrough, D. (2003) Paired plutonic belts in convergent margins and the development of high Sr/Y magmatism: Peninsular Ranges batholith of Baja-California and Median batholith of New Zealand. Geological Society of America Special Paper, 374, 275–296.

Tulloch, A.J., Ramezani, J., Kimbrough, D.L., Faure, K., and Allibone, A.H. (2009) U-Pb geochronology of mid-Paleozoic plutonism in western New Zealand: Implications for S-type granite generation and growth of the east Gondwana margin. Geological Society of America Bulletin, 121, 1236–1261.

Turnbull, I.M., Allibone, A.H., and Jongens, R. (compilers) (2010) Geology of the Fiordland area, New Zealand. GNS Science, Lower Hutt, New Zealand, Institute of Geological and Nuclear Sciences, Geological Map 17, scale 1:250 000, 1 sheet.

Turnbull, R., Tulloch, A., Ramezani, J., and Jongens, R. (2016) Extension-facilitated pulsed S-I-A-type "flare-up" magmatism at 370 Ma along the southeast Gondwana margin in New Zealand: Insights from U-Pb geochronology and geochemistry. Geological Society of America Bulletin, 128, 1500–1520.

Vermeesch, P. (2018) IsoplotR: A free and open toolbox for geochronology. Geoscience Frontiers, 9, 1479–1493.

Vervoort, J.D., Patchett, P.J., Söderlund, U., and Baker, M. (2004) Isotopic composition of Yb and the determination of Lu concentrations and Lu/Hf ratios by isotope dilution using MC-ICP-MS. Geochemistry Geophysics, Geosystems, Q11002.

Wood, B.J., Kiseeva, E.S., and Matzen, A.K. (2013) Garnet in the Earth's mantle. Elements, 9, 421–426.

Yakymchuk, C., and Brown, M. (2014) Behaviour of zircon and monazite during crustal melting. Journal of the Geological Society, 171, 465–479.

Manuscript received January 11, 2021
Manuscript accepted May 19, 2021
Manuscript handled by Callum Hetherington

Endnote:

[1] Deposit item AM-22-67967, Online Materials. Deposit items are free to all readers and found on the MSA website, via the specific issue's Table of Contents (go to http://www.minsocam.org/MSA/AmMin/TOC/2022/Jun2022_data/Jun2022_data.html).